Quantifying the migration rate of drainage divides from high-resolution topographic data

Chao Zhou[1], Xibin Tan[2, *], Yiduo Liu[2], Feng Shi[1, 3]

[1] State Key Laboratory of Earthquake Dynamics, Institute of Geology, China Earthquake Administration, Beijing 100029, China

[2] Key Laboratory of Mountain Hazards and Surface Processes, Institute of Mountain Hazards and Environment, Chinese Academy of Sciences, Chengdu 610299, China

[3] Shanxi Taiyuan Continental Rift Dynamics National Observation and Research Station, Beijing 100029, China

*Corresponding author. E-mail address: tanxibin@imde.ac.cn

Abstract

The lateral movement of drainage divides is co-influenced by tectonics, lithology, and climate, and therefore archives a wealth of geologic and climatic information. It also has wide-ranging implications for topography, the sedimentary record, and biological evolution, thus has drawn much attention in recent years. Several methods have been proposed to determine the drainage divides's migration state (direction and rate), including geochronological approaches (e.g., ^{10}Be) and topography-based approaches (e.g., χ-plots or Gilbert metrics). A key object in these methods is the channel head, which separates the hillslope and channel. However, due to the limited resolution of topography data, the required channel-head parameters in the calculation often cannot be determined accurately, and empirical values are used

in the calculation, which may induce uncertainties. Here, we propose two methods to calculate the migration rate of drainage divides, based on the relatively accurate channel-head parameters derived from high-resolution topographic data. We then apply the methods to an active rift shoulder (Wutai Shan) in the Shanxi rift, and a tectonically stable area (Yingwang Shan) in the Loess Plateau, to illustrate how to calculate drainage-divide migration rates. Our results show that the Wutai Shan drainage divide is migrating northwestward at a rate between 0.21 to 0.27 mm/yr, whereas the migration rates at the Yingwang Shan are approximately zero. This study indicates that the drainage-divide stability can be determined more accurately using high-resolution topographic data. Furthermore, this study takes the cross-divide differences in the uplift rate of channel heads into account in the measurement of drainage-divide migration rate for the first time.

Keywords

Drainage divide; Migration rate; High-resolution topographic data; DEM; Channel head

1. Introduction

The evolution of the Earth's surface is jointly controlled by tectonics, lithology, and climatic conditions (e.g., Molnar and England, 1990; Whipple, 2009; Gallen, 2018; Bernard et al., 2021; Hoskins et al., 2023), providing a basis for reconstructing the past tectonic (Pritchard et al., 2009; Kirby et al.and Whipple, 2012; Shi et al.,

2

2021) or climatic processes (Tucker ~~et al.~~and Slingerland, 1997; Hancock et al., 2002; Schildgen et al., 2022) through topography. The evolution of unglaciated terrestrial terrains is fundamentally coupled with changes in drainage systems through river's vertical (changes in river long profile) and lateral movements (drainage divide migration and river captures) (Whipple, 2001; Clark et al., 2004; Bonnet, 2009; Willett et al., 2014). Previous studies have extensively investigated how river channel profiles respond to tectonic uplift (Whipple, 2001; Crosby and Whipple, 2006; Kirby ~~et al.~~and Whipple, 2012), lithological differences (Duvall et al., 2004; Safran et al., 2005; Forte et al., 2016), and precipitation perturbations (Schlunegger et al., 2011; Bookhagen and Strecker, 2012). River's long profiles have been used to study ~~the~~ earthquake events (e.g., Burbank and Anderson, 2001; Wei et al., 2015) and the spatio-temporal variations of uplift (e.g., Whipple et al., 1999; Kirby et al., 2003; Pritchard et al., 2009; Goren et al., 2014). Recent studies show that the widespread lateral movement of river basins driven by geological and/or climatic disturbance (Yang et al., 2019; Zondervan et al., 2020; Zhou et al., 2022a; Bian et al., 2024) also interacts with the adjustment of channel profiles (Willett et al., 2014). Drainage-divide migration, one form of river lateral movement, may not only carry information on geological and/or climatic disturbance (Su et al., 2020; Zondervan et al., 2020; He et al., 2021; Shi et al., 2021; Zhou et al., 2022a; Zeng and Tan, 2023) but also influence the extraction of tectonic information from channel profiles (Goren et al., 2014; Ma et al., 2020; Jiao et al., ~~2021~~2022). Moreover, it has multi-facet consequences for landscape evolution (Scheingross et al., 2020; Stokes et al.,

20222023), sedimentary processes (Clift & Blusztajn, 2005; Willett et al., 2018; Deng

et al., 2020; Zhao et al., 2021), and biological evolution (Waters et al., 2001; Zemlak

et al., 2008; Hoorn et al., 2010; Musher et al., 20222021). For this reason, the stability

of drainage divides has drawn more and more attention in recent years (e.g.,

Authemayou et al., 2018; Vacherat et al., 2018; Chen et al., 2021; Shelef and Goren,

2021; Sakashita and Endo, 2023; Bian et al., 2024).

Drainage-divide migration is essentially controlled by the cross-divide

difference in erosion and topographic slope (Beeson et al., 2017; Dahlquist et al.,

2018; Chen et al., 2021; Zhou et al., 2022a). The erosion rates are routinely derived

from geochronological techniques, such as cosmogenic nuclides (e.g., ^{10}Be)

concentration measurements (Mandal et al., 2015; Struth et al., 2017; Young and

Hilley, 2018; Sassolas-Serrayet et al., 2019), which can be used to calculate the

migration rates of drainage divides (Beeson et al., 2017; Godard et al., 2019; Hu et al.,

2021). However, these techniques are usually based on samples collected from a

catchment outlet that is several, or even tens of, kilometers away from the drainage

divide and thus may not represent the erosion rates close to the drainage divide

(Sassolas-Serrayet et al., 2019; Zhou et al., 2022a). Besides, the high cost of sample

processing makes it challenging to determine the drainage divide's motion by

measuring the erosion rates throughout the large landscapes. Hence, it would be ideal

to find an accessible and efficient method that can be applied to the entire landscape

and make full use of the ^{10}Be-derived erosion rates.

The advancement of the digital elevation model (DEM) has promoted the

development of geomorphic analysis, making it possible to determine the drainage

divide's transient motion through topography analysis. For example, Willett et al.

(2014) applied the χ method to map the dynamic state of river basins. Forte and

Whipple (2018) proposed the cross-divide comparison of "Gilbert metrics" (including

channel heads' relief, slope, and elevation) to determine a drainage divide's migration

direction. Others adopted the comparison of slope angle or relief of the hillslopes

across a drainage divide to deduce its stability (Scherler and Schwanghart, 2020; Ye et

al., 2022; Zhou et al., 2022b). These geomorphic techniques, so far, could only

determine the migration direction of drainage divides. Braun (2018) provided an

equation that considers both alluvial and fluvial areas to calculate the migration

velocity of an escarpment (also a drainage divide). Zhou et al. (2022a) developed a

technique to calculate the migration rate through the high base-level χ values on both

sides of a drainage divide. These new approaches require channel-head parameters to

calculate the migration rate. However, the location of the channel heads sometimes

cannot be accurately identified because of the limitation in the resolution of DEMs in

natural cases. For this reason, empirical values of channel-head parameters are used in

these studies, which may induce uncertainties.

   This study aims to establish an approach to derive the migration rate of drainage

divides, at a high precision and low cost, based on topographic analysis. We choose a

tectonically active area (i.e., the Wutai Shan in the Shanxi Rift) and a tectonically

inactive area (i.e., the Yingwang Shan in the Loess Plateau) to demonstrate how to

quantify drainage-divide migration rates (Fig. 1). We use the aerial photography

108   acquired by unmanned aerial vehicles (UAVs) and the Structure from Motion (SfM)

109   technology to obtain the high-resolution DEM data of these two areas (0.67 m and

110   0.84 m spatial resolution in the Wutai Shan and the Yingwang Shan, respectively).

111   Benefiting from the high-resolution data, the location of channel heads can be

112   identified more accurately. We then develop two methods to calculate the drainage-

113   divide migration rates. One is based on the measured channel-head parameters, and

114   the other is based on an improved method of Zhou et al (2022a). Combining with the

115   geological and low-temperature thermochronology studies of the Wutai Shan

116   (Middleton et al., 2017; Clinkscales et al., 2020), we also quantify the cross-divide

117   difference in uplift rates to improve the precision of drainage-divide migration rate.

118

2. Methods

2.1 Channel-head-point method

121   According to the detachment-limited stream power model (Howard and Kerby,

122   1983; Howard, 1994), the channel's erosion rate (E) can be expressed as:

$$E = KA^m S^n \tag{1}$$

124   where K is the erosion coefficient, A is the upstream drainage area, S is the gradient of

125   the river channel, and m and n are empirical constants.

126   Because of thresholds such as erosion threshold (the shear stress of overland flow

127   must exceed the threshold of the cohesion of bed material to generate river incision)

128   (Howard and Kerby, 1983; Perron et al., 2008) or landslide threshold (landslides

129 occur when the threshold of soil or rock strength is exceeded in high relief region)

130 (Burbank et al., 1996; Tucker and Bras~~et al.~~, 1998), river channels (following Eq. 1)

131 emerge at a certain distance from the drainage divide. The region between the channel

132 head and the drainage divide is referred to as the hillslope area, where the erosion is

133 controlled by landslide, collapse, and diffusion processes (Carson and Kirkby, 1972;

134 Stock~~e~~ and Dietrich, 2006; Stark, 2010; Braun et al., 2018; Dahlquist et al., 2018).

135 The channel-head point is the highest and the closest point to the drainage divide on a

136 river channel (Clubb et al., 2014). Therefore, the erosion rate at channel-head points

137 (E_{ch}) can be described as:

$$E_{ch} = KA_{cr}^m S_{ch}^n \tag{2}$$

139 where E_{ch} is the erosion rate at channel-head points, A_{cr} is the critical upstream

140 drainage area of a channel-head point (Duvall et al., 2004; Wobus et al., 2006), and

141 S_{ch} is the channel-head gradient measured along the channel near the channel-head

142 point. Eq. 2 indicates that the side of a drainage divide with a higher A_{cr} or S_{ch} can

143 have a higher erosion rate than the other side, and is more likely to pirate the opposite

144 drainage basin. Besides, a high erosion coefficient can amplify the drainage basin's

145 erosion rate.

146   Drainage-divide migration is essentially controlled by the cross-divide difference

147 in erosion rates and topographic slope (Beeson et al., 2017; Dahlquist et al., 2018;

148 Chen et al., 2021; Zhou et al., 2022a; Stokes et al., ~~2022~~2023). Furthermore, the

149 differential uplift should also be considered when using the cross-divide erosion rates

150 at the channel heads to calculate the erosion difference across the divide, especially in

151 the case of tectonic tilting uplift (Zhou et al., 2022a). The drainage-divide migration

152 rate (D_{mr}) can be obtained according to the cross-divide difference in erosion rate and

153 uplift rate and the slopes across the divide (Zhou et al., 2022a):

154
$$D_{mr} = \frac{\Delta E_{ch} - \Delta U_{ch}}{\tan\alpha + \tan\beta} \tag{3}$$

155 where ΔE_{ch} is the difference in erosion rate between the two sides (annotated as α and

156 β) of the drainage divide ($\Delta E_{ch} = E_{ch\alpha} - E_{ch\beta}$). The choice of α or β is arbitrary, and

157 the positive direction of the migration rate is assigned from the α to the β side whereas

158 the negative is the opposite. ΔU_{ch} is the cross-divide difference in uplift rate (ΔU_{ch} =

159 $U_{ch\alpha} - U_{ch\beta}$), and tan$\alpha$ and tanβ are the average gradients (along the normal-divide

160 direction) upslope of the channel head (not including the hilltop part) on the αeach

161 side and the β side, respectively of the drainage divide. Assuming the erosion

162 coefficient (K) is the same on both sides of a drainage divide, Eqs. 2 and 3 allow us to

163 derive the equation of drainage divide's migration rate according to the parameters at

164 the channel-head points:

165
$$D_{mr} = \frac{K\left[\left(A_{cr}^m S_{ch}^n\right)_\alpha - \left(A_{cr}^m S_{ch}^n\right)_\beta\right] - \Delta U_{ch}}{\tan\alpha + \tan\beta} \tag{4}$$

166   If the exact value of K is unknown, the drainage divide's unilateral erosion rate

167 can be used as a substitution:

168
$$D_{mr} = \frac{E_\alpha\left[1 - \frac{\left(A_{cr}^m S_{ch}^n\right)_\beta}{\left(A_{cr}^m S_{ch}^n\right)_\alpha}\right] - \Delta U_{ch}}{\tan\alpha + \tan\beta} \tag{5}$$

169 or:

170
$$D_{mr} = \frac{E_\beta\left[\frac{\left(A_{cr}^m S_{ch}^n\right)_\alpha}{\left(A_{cr}^m S_{ch}^n\right)_\beta} - 1\right] - \Delta U_{ch}}{\tan\alpha + \tan\beta} \tag{6}$$

171 E_α and E_β are the erosion rates of the α and the β side of the drainage divide,

8

172 respectively, which can be derived through cosmogenic nuclides (^{10}Be) concentration

173 measurements (Beeson et al., 2017; Godard et al., 2019; Hu et al., 2021). The regional

174 average erosion rate ($\bar{E} = \frac{E_\alpha + E_\beta}{2}$) can also be used to calculate the migration rate:

$$D_{mr} = \frac{2\bar{E}\left|\frac{(A_{cr}^m S_{ch}^n)_\alpha - (A_{cr}^m S_{ch}^n)_\beta}{(A_{cr}^m S_{ch}^n)_\alpha + (A_{cr}^m S_{ch}^n)_\beta}\right| - \Delta U_{ch}}{tan\alpha + tan\beta} \tag{7}$$

176 Based on Eqs. 4-7, the migration rate of drainage divides can be estimated using

177 channel-head parameters combined with one of the erosion-related parameters,

178 erosion coefficient (K), erosion rate at one side of a drainage divide (E_α or E_β), or

179 regional average erosion rate ($\bar{E}$).

180

181

2.2 Channel-head-segment method

183 A channel-head segment is the channel segment just below the channel head

184 (Zhou et al., 2022a). Zhou et al. (2022a) developed a method based on the cross-

185 divide χ contrast of channel-head segments to calculate the migration rate of drainage

186 divides. The essence of the method is the cross-divide comparison of the channel-

187 head segments' normalized channel steepness (k_{sn}) values. k_{sn} is a widely used index

188 (Whipple et al., 1999; Wobus et al., 2006; Hilley and Arrowsmith, 2008; Kirby and

189 Whipple, 2012) that is quantitatively related to E and K ($k_{sn} = \left(\frac{E}{K}\right)^{\frac{1}{n}}$). χ is an integral

190 function ($\chi = \int_{x_b}^{x} \left(\frac{A_0}{A(x)}\right)^{\frac{m}{n}} dx$) of a channel's upstream area (A) to horizontal distance

191 (x) (Royden et al., 2000; Perron and Royden, 2012), and A_0 is an arbitrary scaling area

192 to make the integrand dimensionless.

9

193   In the method of Zhou et al. (2022a), the location of channel heads cannot be

194   accurately identified, because it is limited by the resolution of DEM. Therefore, an

195   empirical value of $A_{cr} = 10^5$ m^2 was used in the calculation. Benefiting from the high-

196   resolution DEM in this study, we improve the method in Zhou et al. (2022a) and use

197   the real location of channel heads to calculate the migration rate. When the regional

198   erosion coefficient (K) is known and unchanged in the vicinity of the drainage divide,

199   the drainage-divide migration rate can be estimated by the following equation:

200
$$D_{mr} = \frac{K\left[k_{sn(\alpha)}{}^n - k_{sn(\beta)}{}^n\right] - \Delta U_{ch}}{tan\alpha + tan\beta} = \frac{K\left\{\left[\frac{(z_{ch}-z_b)_\alpha}{\chi_\alpha}\right]^n - \left[\frac{(z_{ch}-z_b)_\beta}{\chi_\beta}\right]^n\right\} - \Delta U_{ch}}{tan\alpha + tan\beta} \tag{8}$$

201   where z_{ch} ~~and z_b are~~is the elevation~~s~~ of the channel head~~s~~, ~~and~~z_b is the elevation of

202   catchment outlet~~s~~ (at the top part of the channel to make the elevation-χ profiles

203   quasi-linear between the channel head and the outlet), and subscripts α and β denote

204   the two rivers across a divide~~, respectively~~. The detailed derivation of Eq. 8 is in

205   Supplementary Materials. The drainage divide's unilateral erosion rate (E_α or E_β) can

206   also be used as a substitution for the K value:

207
$$D_{mr} = \frac{E_\alpha\left\{1 - \left(\frac{\chi_\alpha}{\chi_\beta}\right)^n \left[\frac{(z_{ch}-z_b)_\alpha}{(z_{ch}-z_b)_\beta}\right]^{-n}\right\} - \Delta U_{ch}}{tan\alpha + tan\beta} \tag{9}$$

208   or:

209
$$D_{mr} = \frac{E_\beta\left\{\left(\frac{\chi_\alpha}{\chi_\beta}\right)^{-n} \left[\frac{(z_{ch}-z_b)_\alpha}{(z_{ch}-z_b)_\beta}\right]^n - 1\right\} - \Delta U_{ch}}{tan\alpha + tan\beta} \tag{10}$$

210   Alternatively, one can use the regional average erosion rate ($\bar{E}$) to calculate the

211   migration rate:

212
$$D_{mr} = \frac{2\bar{E}\left\{\frac{\left[\frac{(z_{ch}-z_b)_\alpha}{(z_{ch}-z_b)_\beta}\right]^n - \left(\frac{\chi_\alpha}{\chi_\beta}\right)^n}{\left[\frac{(z_{ch}-z_b)_\alpha}{(z_{ch}-z_b)_\beta}\right]^n + \left(\frac{\chi_\alpha}{\chi_\beta}\right)^n}\right\} - \Delta U_{ch}}{tan\alpha + tan\beta} \tag{11}$$

213 Based on Eqs. 8-11, the drainage-divide migration rate can be estimated using the χ

214 values of high-base-level channel segments combined with one of the erosion-related

215 parameters, erosion coefficient (K), erosion rate at one side of a drainage divide (E_α or

216 E_β), or regional average erosion rate ($\bar{E}$).

217

2.3 Parameter extraction

219   In this study, —we apply the erosion coefficient (K) related equations (Eqs. 4 &

220 8) to two natural examples in North China, the Wutai Shan in the Shanxi Rift and the

221 Yingwang Shan in the Loess Plateau, to demonstrate how to calculate the drainage-

222 divide migration rates (Fig. 1). We calculated the K, according to the equation, $K =$

223 $\frac{E}{k_{sn}{}^n}$, the erosion rate obtained by chronological methods, the k_{sn}, and the assumed

224 slope exponent ($n = 1$). The k_{sn} is calculated based on S and A ($k_{sn} = SA^{\frac{m}{n}}$) extracted

225 from ALOS DEM (downloaded from https://search.asf.alaska.edu/) using

226 TopoToolbox (Schwanghart and Scherler, 2014), and the interpolation uses the

227 Kriging method on ArcGIS (Fig. 2).

228   We use a small four-rotor Unmanned Aerial Vehicle (UAV), the DJI Phantom 4,

229 to acquire stereo images of the areas. Based on the Structure-from-Motion (SfM)

230 method and PhotoScan software, we obtained the DEMs with a spatial resolution of

231 0.67 m in the Wutai Shan and 0.84 m in the Yingwang Shan~~UAV acquired aerial~~

232 ~~photography and structure from motion (SfM) photogrammetry to derive the high-~~

233 ~~resolution DEM of the two study areas, the Wutai Shan in the Shanxi Rift, and the~~

234 ~~Yingwang Shan in the Loess Plateau~~ (can be download from

235 https://doi.org/10.5069/G98C9TGT)~~, both located in North China (Fig. 1)~~. Both

236 regions are semi-arid, and the vegetation is dominated by shrubs. We did not compare

237 the elevations to the standard GPS points, which may bring errors on the elevations.

238 ~~The spatial resolution is 0.67 m in the Wutai Shan, and 0.84 m in the Yingwang Shan.~~

239 Based on the high-resolution topography data, we first extract river channels and

240 drainage divide, using a single-flow-direction algorithm (D8). Then we extract the

241 relevant parameters, ~~-~~and calculate the drainage-divide migration rate ~~using the two~~

242 ~~methods above for each case~~. Data a~~A~~nalysis ~~of the data~~including *the calculation of*

243 *channel steepness (k_{sn}), the creation of* slope-area plots, χ-plots, ~~and the extraction~~

244 river's long profiles and topographic swath profiles, ~~is~~ are based on the Matlab

245 toolbox TAK (Forte and Whipple, 2019) and TopoToolbox (Schwanghart and

246 Scherler, 2014). According to the breaking point of the slope-area regression line, we

247 obtain the value of the critical upstream drainage area (A_{cr}) of each river channel ~~The~~

248 ~~kriging interpolation of k_{sn} and the generation of the k_{sn} distribution map are based on~~

249 ~~the ArcGIS software.~~

250

251 (Duvall et al., 2004). According to these values, we mark the position (and its

252 elevation, z_{ch}) of the channel heads on the χ-plots and the topography map. An

253 elevation of the catchment outlet (z_b) can be assigned at the top part of the channel to

make the elevation-χ profiles quasi-linear between the channel head and the outlet.

The slope of the channel head (S_{ch}) is calculated, according to the 100 m long channel

on the river's long profiles around the channel head (50 m upstream and downstream).

Topographic gradient ($\tan\alpha$ or $\tan\beta$) is calculated through the average slope (in the

normal-divide direction) of the hillslope segment (not including the hilltop part,

because of its lower gradient). The cross-divide uplift difference in the channel-head

points (ΔU_{ch}) is estimated according to the location of the each channel head and the

tectonic uplift trend.

3. Applications to natural cases

We apply the new methods to two natural examples in North China, the Wutai

Shan in the Shanxi Rift and the Yingwang Shan in the Loess Plateau, to demonstrate

how to calculate the drainage-divide migration rates (Fig. 1).
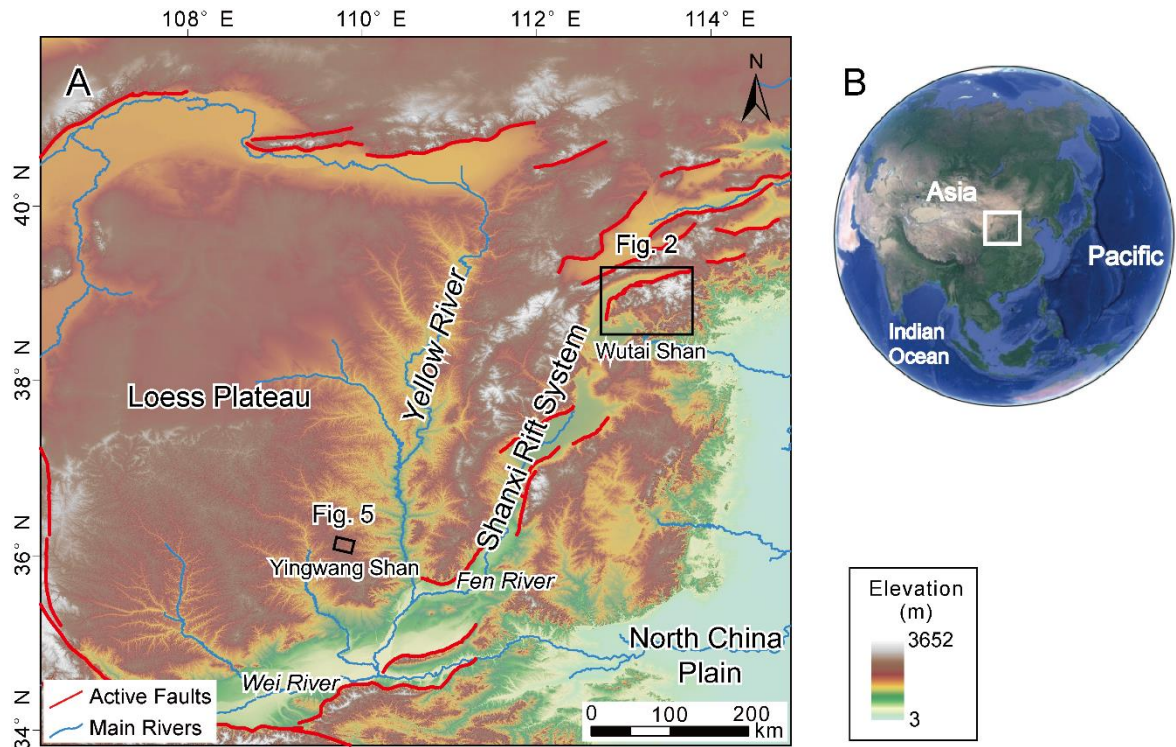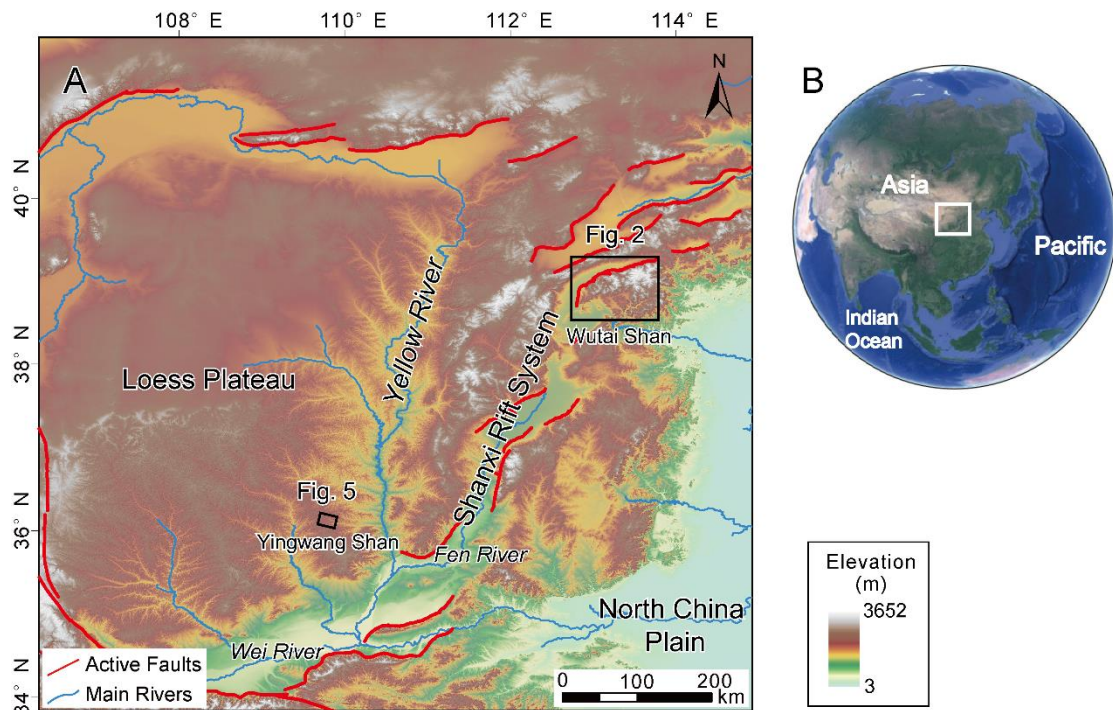
Figure 1. Locations and tectonic background of the two nature cases in North China. The figure is modified from Fig. 7 in Shi et al. (2021). (**A**) Red lines represent the main active faults. Black rectangles show the locations of the two nature cases. Red curve denotes active fault, sourced from https://www.activefault-datacenter.cn/. The

14

273   topography data (ALOS DEM, ~~12.5 m resolution~~) is downloaded from the Alaska

274   Satellite Facility (ASF) Data Search (https://search.asf.alaska.edu/). (**B**) The satellite

275   image downloaded from Google Earth. White rectangles show the location of Panel

276   A.

277

3.1 Wutai Shan

279   The Wutai Shan is a tilted fault block on the shoulder of the Shanxi Rift System

280   located in the central North China craton (Fig. 1) (Xu et al., 1993; Su et al., 2021).

281   The tilting uplift of the Wutai Shan is controlled by the Northern Wutai Shan fault,

282   and there is no active fault along the south edge of the Wutai Shan horst (Fig. 2). The

283   bedrock of the Wutai Shan area consists mainly of metamorphic and igneous

284   basement rocks (Clinkscales et al., 2020) and there is no obvious variation in rock

285   erodibility and precipitation in this area (Fig. S2 & S3). Zhou et al. (2022b) reveal that

286   the Wutai Shan drainage divide is migrating northwestward due to the tilting uplift

287   and predicts the drainage divide will move ~10 km to the northwest to achieve a

288   steady state if all geological conditions remain. Geomorphic evidence also exhibits a

289   northwestward migration of the drainage divide (Fig. 3). The plan and satellite views

290   show several abnormally high junction angles~~barbed tributaries and a captured area~~

291   around the Wutai Shan drainage divide, which indicate that the tributaries formerly

292   part of the northern drainage have become part of the southern drainage (Fig. 3A&B).

293   The χ-plots analysis shows the southern side of the drainage divide has steeper

294   channels, higher k_{sn}, and lower χ. The χ-plots of paired rivers illustrate obvious

295   characteristics of shrinking-expanding and captured-beheaded rivers (Fig. 3C).

296   To derive the erosion coefficient of the Wutai Shan area, we calculate the

297   channel steepness (k_{sn}) of this region, assuming $n = 1$ and $m = 0.45$ (Wobus et al.,

298   2006; DiBiase et al., 2010; Perron and Royden, 2012; Wang et al., 2021). We then use

299   the Kriging interpolation method to generate the k_{sn} distribution map (Fig. 2B). In

300   addition, results under the assumptions of $m = 0.35$ and 0.55, respectively, are shown

301   in Supplementary Materials (Fig. S4). The average k_{sn} value of the upthrown side near

302   the Northern Wutai Shan fault is ~80 $m^{0.9}$ (Fig. 2D). Middleton et al. (2017) showed

303   that ~~Previous geological study shows that~~ the Quaternary throw rates of the Northern

304   Wutai Shan fault are 0.8-1.6 mm/~~ay~~r ~~(Middleton et al., 2017)~~. ~~The~~Clinkscales et al.

305   (2020) showed, using low-temperature thermochronology, ~~study shows~~ that the time-

306   averaged long-term throw rates in the late Cenozoic is about 0.25 mm/yr, and there is

307   an accelerated activity in the Wutai Shan area ~~(Clinkscales et al., 2020)~~. According to

308   these studies, we assume a 0.50 ± 0.25 mm/yr uplift/erosion rate in the northern

309   margin of the Wutai Shan (in the footwall of the Northern Wutai Shan fault).

310   Combining with the equation, $K = \frac{E}{k_{sn}{}^n}$, and following the approach of previous

311   studies (Kirby and Whipple, 2001; Kirkpatrick et al., 2020; Ma et al., 2020), the

312   erosion coefficient (K) is calculated to be $(6.25 \pm 3.13) \times 10^{-6}$ $m^{0.1}yr^{-1}$ in this area.

313   Because there is no obvious variation in rock erodibility and precipitation in this area

314   (Figs. S2 & S3), we use this value as the erosion coefficient (K) of the Wutai Shan

315   area.

316   We then apply the two new methods (Eqs. 4 & 8) to calculate the migration rate

317   of the drainage divide in the Wutai Shan. We first choose three pairs of rivers (Fig.

318   4A) and acquire their slope-area plots (Figs. 4B, E, H) and the χ-plots (Figs. 4C, F, I).

319   ~~According to the location of the catchment outlets (Fig. 4A), we obtain the outlet~~

320   ~~elevations (z_b) from the river's long profiles.~~ According to the breaking point of the

321   slope-area regression line (Duvall et al., 2004) (Figs. 4B, E, H), we obtain the values

322   of the critical upstream drainage area (A_{cr}). According to these values, we separate

323   hillslope and channel areas and mark the position of the channel heads on the χ-plots

324   and the topography map (Fig. 4A). For the χ-plots (Figs. 4C, F, I), we obtain the

325   elevations of channel heads (z_{ch}) and χ values based on the coordinate of the channel-

326   head points. According to the location of the channel heads on the river's long

327   profiles, we calculate the ~~slope of the channel heads' tangent lines, and derive the~~

328   channel-head gradient (S_{ch}). Topographic gradient ($\tan\alpha$ or $\tan\beta$) is calculated through

329   the average slope (in the normal-divide direction) of the hillslope

330   segment~~Topographic gradient ($\tan\alpha$ or $\tan\beta$) is calculated through the average slope of~~

331   ~~the hillslope segment near the channel head (Stokes et al., 2022)~~ (not including the

332   hilltop part, Figs. 4D, G, J).

333   ~~If~~According to the previous studies (Middleton et al., 2017; Clinkscales et al.,

334   2020) and the k_{sn} distribution (Fig. 2D), we assume the rock uplift rate decreases

335   linearly from 0.5 to 0 mm/yr from northwest to southeast of the Wutai Shan horst

336   (~40 km wide~~), .~~). Then we can obtain that ~~the~~ the cross-divide uplift difference in the

337   channel-head points (ΔU_{ch}) (the distance perpendicular to the direction of the

17

338   boundary fault is ~600 m) is ~0.008 mm/yr. After determining these parameters, we

339   adopt the channel-head-point (Eq. 4) and channel-head-segment (Eq. 8) methods,

340   respectively, to calculate the migration rates. The required data for calculation and the

341   migration rates are shown in Table 1. The calculated results for m/n = 0.35 and 0.55,

342   respectively, are shown in Supplementary Materials (Table S1). The migration rates

343   are higher when m/n = 0.35 and lower when m/n = 0.55, which indicates the m/n value

344   is sensitive to the result.

345   The rivers have different characteristics on both sides of the drainage divide, as

346   illustrated on their slope-area plots (Figs. 4B, E, H) and the χ-plots (Figs. 4C, F, I).

347   For the first site (Fig. 4D), the migration rates calculated by the channel-head-point

348   and channel-head-segment methods are 0.21 mm/yr and 0.26 mm/yr, respectively. For

349   the second site (Fig. 4G), the migration rates are 0.23 mm/yr and 0.27 mm/yr,

350   respectively. For the third site (Fig. 4J), 0.21 mm/yr and 0.22 mm/yr, respectively. The

351   drainage divides of all three points are migrating northwestward, which is consistent

352   with the previous result inferred by the cross-divide contrast of slopes in this area

353   (Zhou et al., 2022b). Furthermore, the migration rates calculated by the two methods

354   are comparable in all three sites.

355
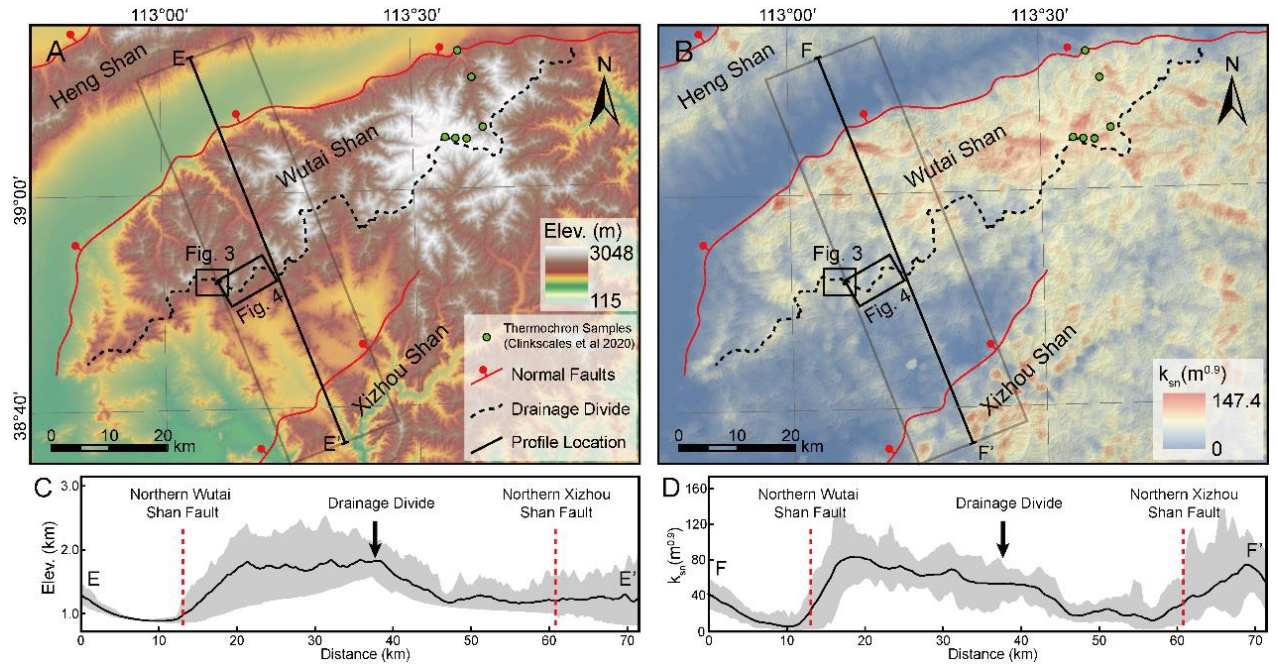
Figure 2. Topography (**A**) and normalized channel steepness (k_{sn}) (**B**) distribution of

the Wutai Shan horst and surrounding area in the Shanxi Rift System. The black

dashed line shows the location of the main drainage divide. Red lines show the main

active faults. The black lines show the location of profiles E-E' and F-F'. Black

rectangles show the area of Fig. 3B & 4A. Gray boxes show the area of the swath

profiles in Panels C and D. Green dots denote the locations of the low-temperature

thermochronology samples in Clinkscales et al. (2020). ~~The topography data (ALOS~~

~~DEM, 12.5 m resolution) is downloaded from the Alaska Satellite Facility (ASF) Data~~

~~Search (https://search.asf.alaska.edu/).~~ The k_{sn} is calculated based on S and A extracted

from ALOS DEM ($k_{sn} = SA^{\frac{m}{n}}$) and a uniform m/n (0.45) using TopoToolbox

(Schwanghart and Scherler, 2014), and the interpolation uses the Kriging method on

ArcGIS. (**C**) Topography swath profile along E-E'. See location in Panel A. (**D**) k_{sn}

swath profile along F-F'. See location in Panel B. The swath profiles are extracted

using TopoToolbox (Schwanghart and Scherler, 2014). The red dashed lines show the

371   location of the main active normal faults, and the black arrow shows the location of

372   the main drainage divide. Both swath profiles are 20 km wide (10 km on each side).

373
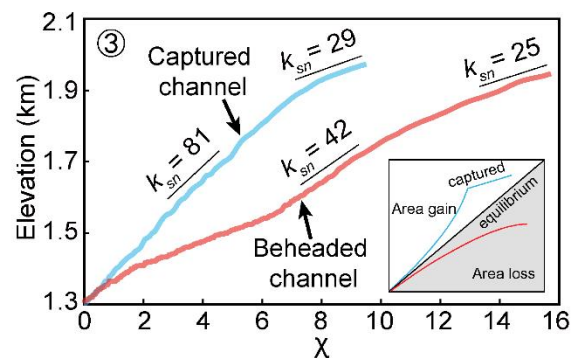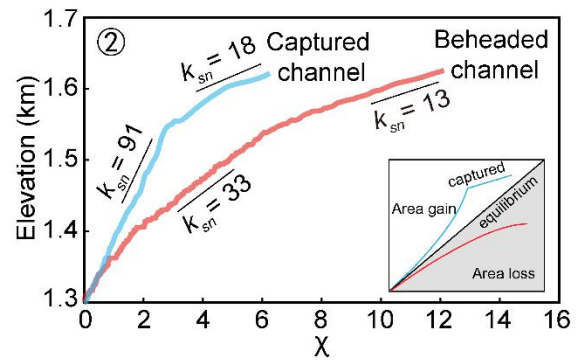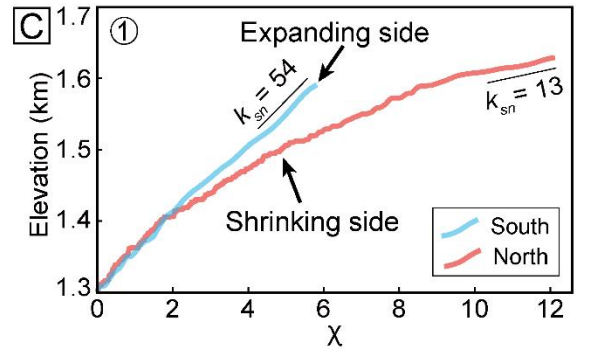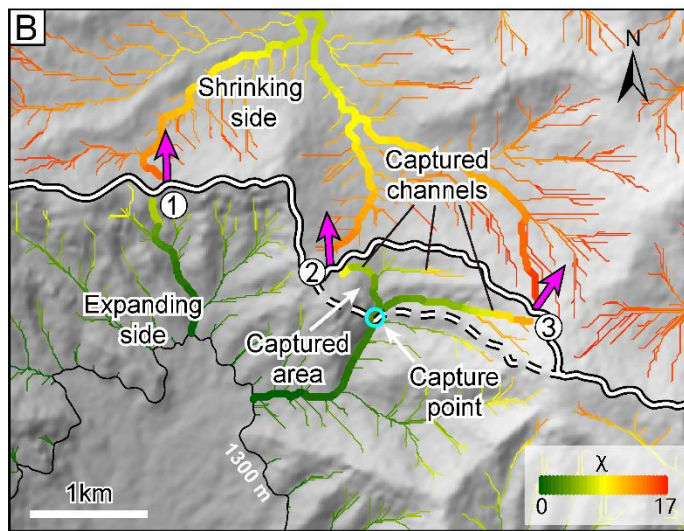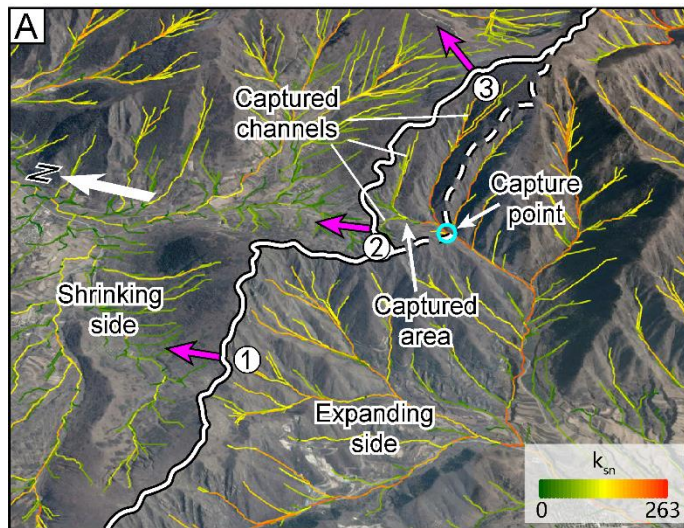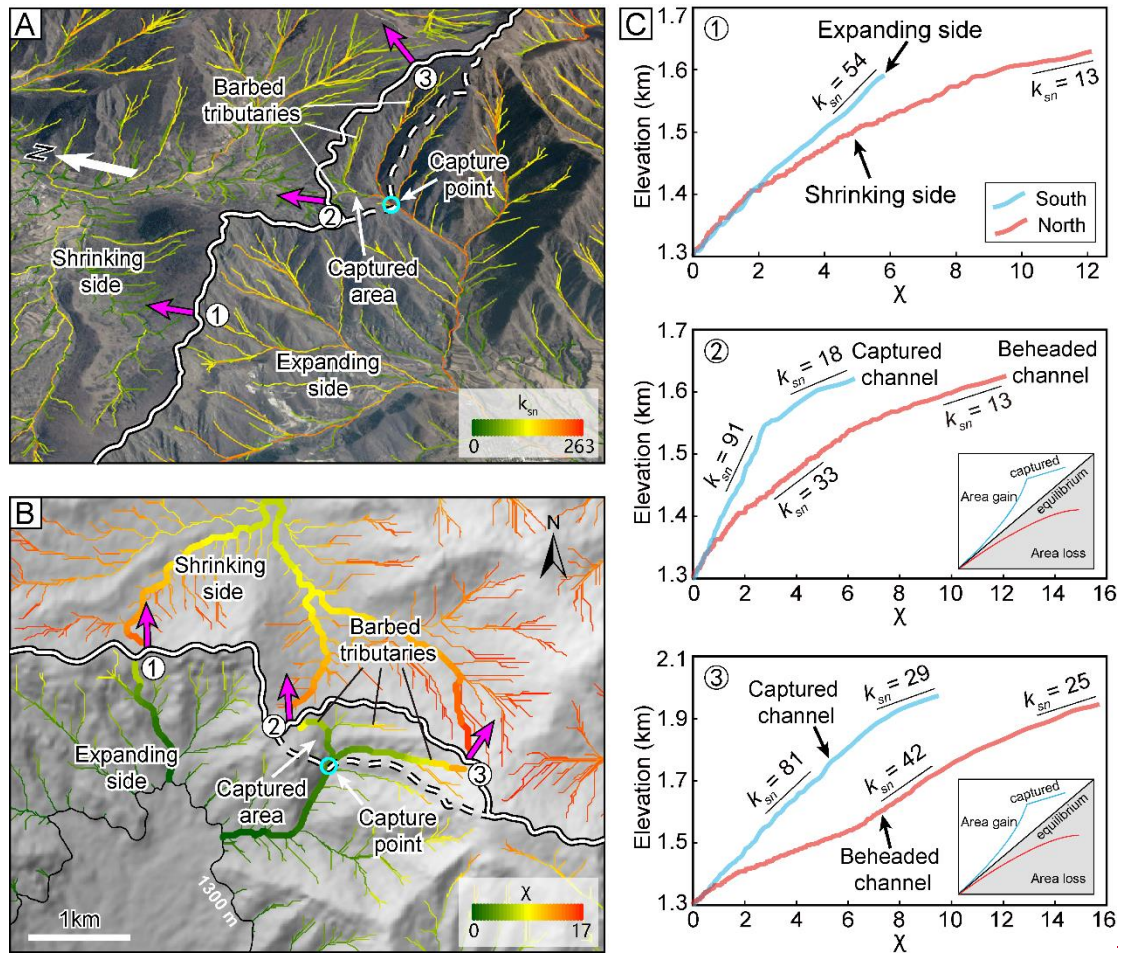
Figure 3. Perspective views and χ map of the drainage divide in the Wutai Shan (see

Fig. 2 for location). (A) Perspective views of a captured area and the channels mapped

with k_{sn}. The south side of the drainage divide has steeper channels and higher k_{sn} than

the north side. Magenta arrows show drainage divide migration directions. The

satellite image is from Google Earth. (B) χ map of this area with the outlet elevation

of 1300 m. The south side of the drainage divide has lower χ values than the north

side. It should be noted that the catchment outlet at the north side of the drainage

basins (the 1300 m contour) is out of the map. The χ-plots of the rivers in bold lines

are shown in Panel C. ~~The topography data (ALOS DEM, 12.5 m resolution) is~~

~~downloaded from the Alaska Satellite Facility (ASF) Data Search~~

~~(https://search.asf.alaska.edu/).~~ (C) χ-plots of the three paired rivers in Panel B. The blue

21

387   and red curves correspond to the rivers on the south and north sides, respectively. The

388   χ-plot of River 1 is steeper on the south side, indicating that the river on the south side

389   is expanding and the river on the north side is shrinking. The χ-plots of Rivers 2 and 3

390   in the captured area show obvious characteristics of the captured and beheaded rivers.

391   The χ-plot is extracted using TAK (Forte and Whipple, 2019) and TopoToolbox

392   (Schwanghart and Scherler, 2014).

393
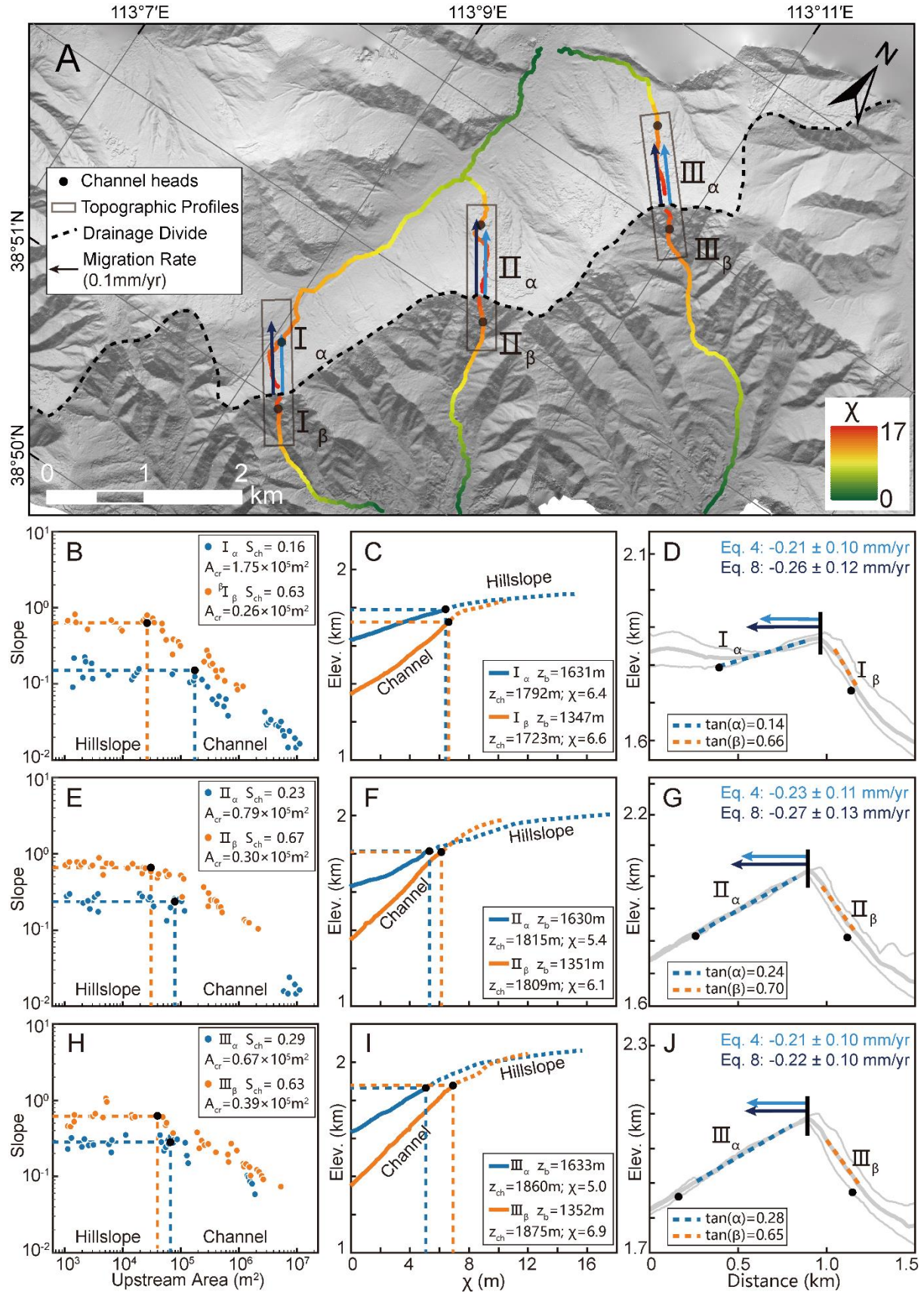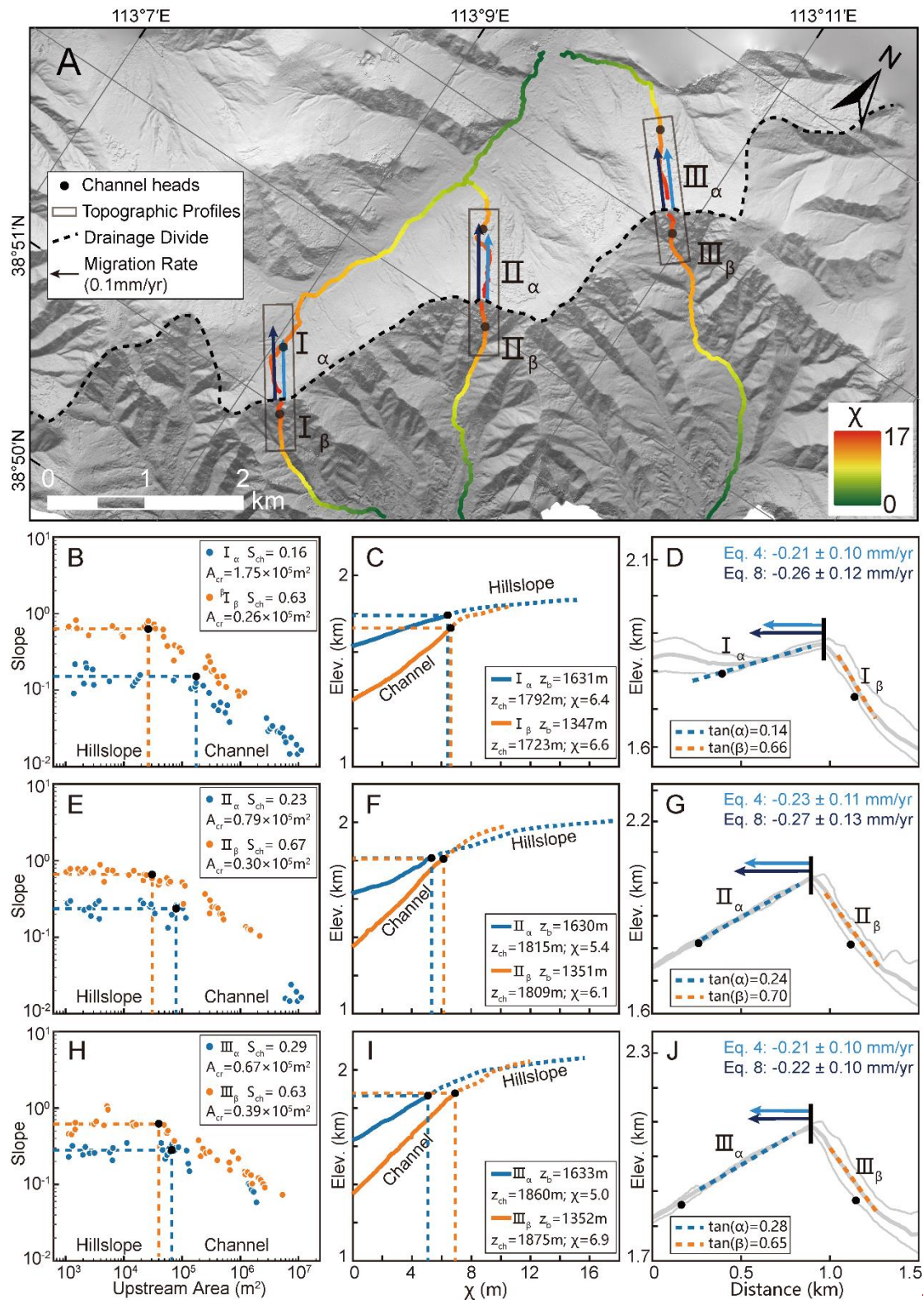
Figure 4. Analytical results of the Wutai Shan drainage divide. (**A**) High-resolution

hill-shade map (0.67 m spatial resolution) of the Wutai Shan. The black dashed line

shows the location of the main drainage divide. Colored lines show the three pairs of

selected channels used for analysis. The black dots are the channel heads. Black

rectangles show the location of the cross-divide topography swath profiles. The black

arrows show the direction of drainage-divide migration (**B, E, H**) Slope-area plots of

the three pairs of selected channels. The blue and orange dots are the slope-area plots

of the north (α) and south (β) sides of the drainage divide respectively. The black dots

represent the channel heads. (**C, F, I**) χ-plots of the selected channels. The blue and

orange lines are the χ-plots of the north (α) and south (β) sides of the drainage divide

respectively. The black dots represent the channel heads. (**D, G, J**) Cross-divide

topography swath profiles with the drainage-divide migration rates. The locations of

the profiles are in Panel A. The light and dark blue arrows are the drainage-divide

migration rates calculated by the channel-head-point (Eq. 4) and channel-head-

segment (Eq. 8) methods respectively.

3.2 Yingwang Shan

The Loess Plateau is hosted by the tectonically stable Ordos Block of the North

China craton (Yin, 2010; Su et al., 2021). Over the past 2.6 million years, it has

accumulated tens to hundreds of meters of eolian sediments (Yan et al., 2014),

draping preexisting topography (Xiong et al., 2014). There is no active fault and little

to no variation in rock erodibility and precipitation within the area (Shi et al., 2020;

Zhou et al., 2022b).

We apply the two methods to Yingwang Shan of Loess Plateau to calculate the

420 drainage-divide migration rate. Similar to the Wutai Shan site, we obtain the slope-

421 area plots (Figs. 5 B, E, H), the χ-plots (Figs. 5 C, F, I), and extract the values of A_{cr},

422 S_{ch}, z_b, z_{ch}, χ, $\tan\alpha$ and $\tan\beta$ of the rivers. The rate of soil erosion in the study area is

423 about 500 t·km^{-2}yr^{-1} according to the distribution of silt discharge (Fu, 1989).

424 Combining with the assumption of the density of loess, 1.65 t·m^{-3}, the present-day

425 erosion rate in the study area is calculated to be 0.3 mm·yr^{-1}. Because there is no

426 obvious unequal uplift in this region, we assign that ΔU_{ch} is zero. We also assume $n =$

427 1 and $m = 0.45$ in the calculation (Wobus et al., 2006; DiBiase et al., 2010; Perron and

428 Royden, 2012; Wang et al., 2021). Then, we use the methods of channel-head

429 parameters (Eq. 7) and channel segments (Eq. 11) to calculate the drainage-divide

430 migration rates. The required data for calculation and the migration rates are shown in

431 Table 1.

432   All results of the three points show that the drainage-divide migration rate here is

433 close to zero, no matter which method is used in the calculation. The results show that

434 the drainage divide of the study site is in topographical equilibrium, which is

435 consistent with the inference in previous studies (Willett et al., 2014, Zhou et al.,

436 2022b).

437
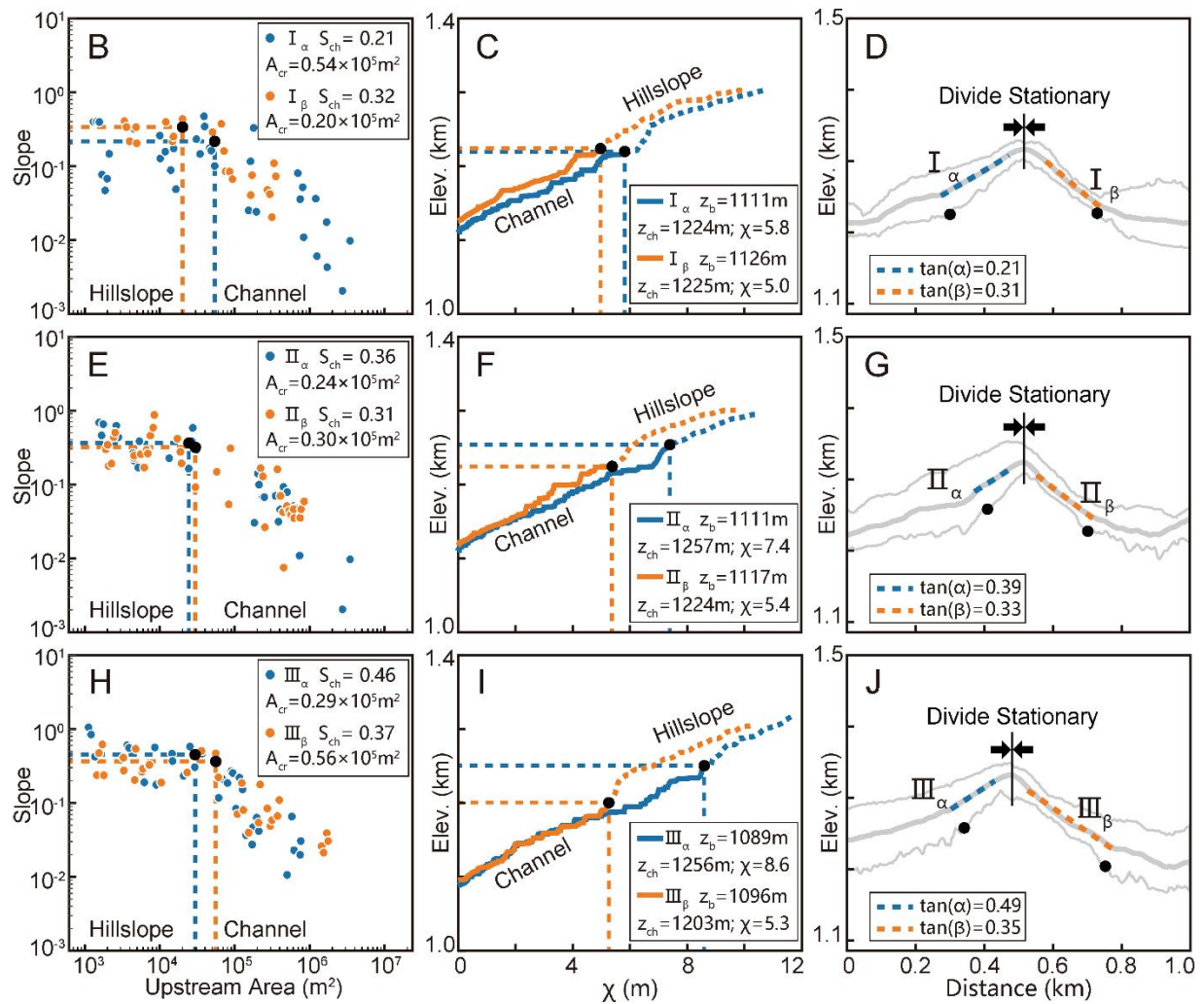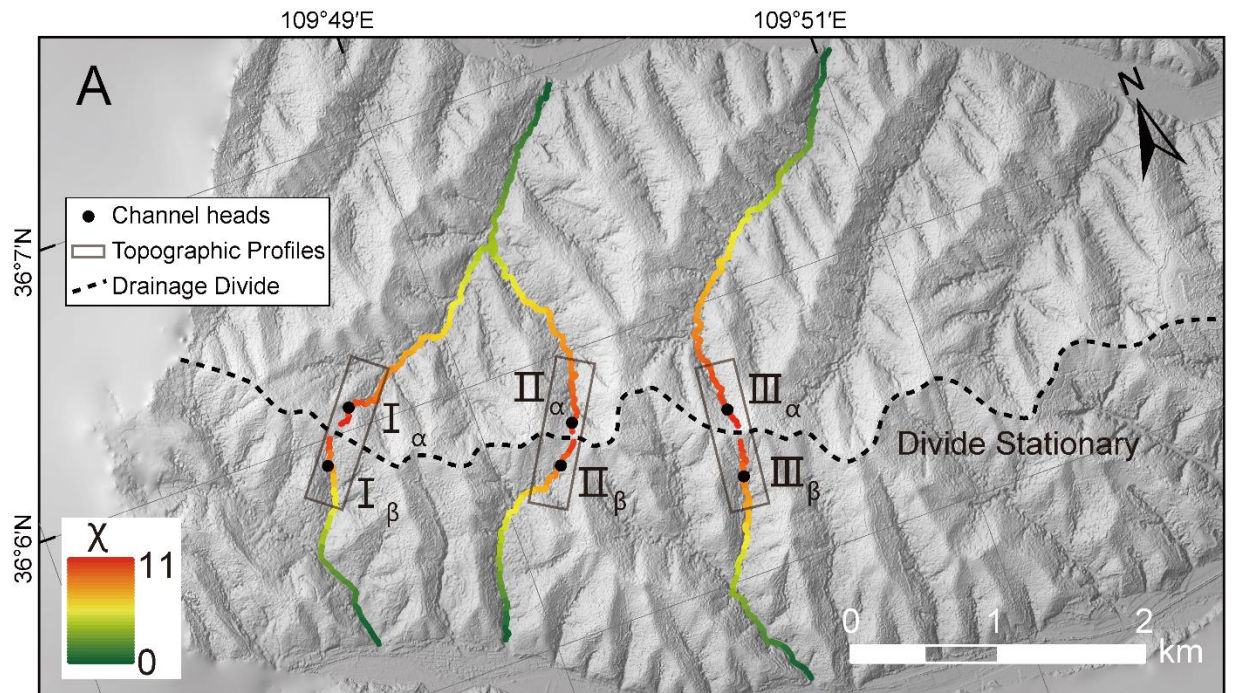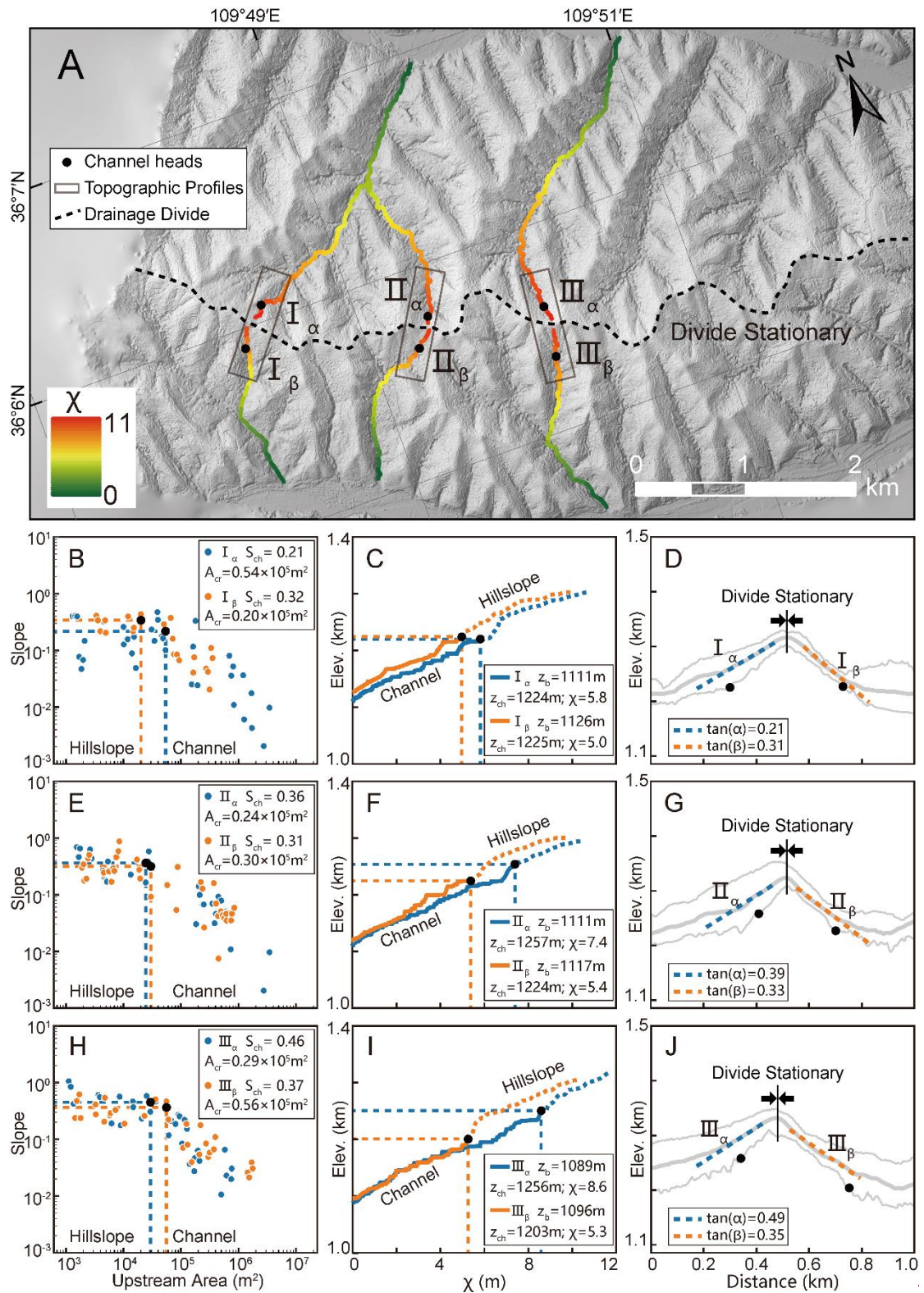
Figure 5. Analytical results of the Yingwang Shan in the Loess Plateau. (**A**) High-

resolution hill-shade map (0.84 m spatial resolution). The black dotted line shows the

location of the main drainage divide. Colored lines show the three pairs of selected

443   channels used for analysis. The black dots represent the channel heads. Black

444   rectangles show the location of the cross-divide topography swath profiles. (**B, E, H**)

445   Slope-area plots of the three pairs of selected channels. The blue and orange dots are

446   the data of the north (α) and south (β) sides of the drainage divide respectively. The

447   black dots represent the channel heads. (**C, F, I**) χ-plots of the selected channels. The

448   blue and orange lines are the χ-plots of the north (α) and south (β) sides of the

449   drainage divide respectively. The black dots represent the channel heads. (**D, G, J**)

450   The cross-divide topography swath profiles. The locations of the swath profiles are in

451   Panel A.

452

453 **Table 1**. Channel parameters and migration rates of drainage divides in two field cases.

Natural Cases	No.	A_{cr} ($\times10^5$m^2)	S_{ch}	z_b (m)	z_{ch} (m)	χ	$\tan\alpha$	$\tan\beta$	ΔU_{ch} (mm/yr)	D_{mr} (mm/yr) (Channel-head-point method)	D_{mr} (mm/yr) (Channel-head-segment method)
Wutai Shan	Fig. 4 I$_\alpha$	1.75	0.16	1631	1792	6.4	0.14	0.66	~ 0.008	-0.21±0.10	-0.26±0.12
	Fig. 4 I$_\beta$	0.26	0.63	1347	1723	6.6					
	Fig. 4 II$_\alpha$	0.79	0.23	1630	1815	5.4	0.24	0.70	~ 0.008	-0.23±0.11	-0.27±0.13
	Fig. 4 II$_\beta$	0.30	0.67	1351	1809	6.1					
	Fig. 4 III$_\alpha$	0.67	0.29	1633	1860	5.0	0.28	0.65	~ 0.008	-0.21±0.10	-0.22±0.10
	Fig. 4 III$_\beta$	0.39	0.63	1352	1875	6.9					
Yingwang Shan	Fig. 5 I$_\alpha$	0.54	0.21	1111	1224	5.8	0.21	0.31	0	~ 0.03	~ -0.01
	Fig. 5 I$_\beta$	0.20	0.32	1126	1225	5.0					
	Fig. 5 II$_\alpha$	0.24	0.36	1111	1257	7.4	0.39	0.33	0	~ 0.02	~ -0.01
	Fig. 5 II$_\beta$	0.30	0.31	1117	1224	5.4					
	Fig. 5 III$_\alpha$	0.29	0.46	1089	1256	8.6	0.49	0.35	0	~ 0.02	~ -0.01
	Fig. 5 III$_\beta$	0.56	0.37	1096	1203	5.3					

454

4. Discussion

4.1 Location of channel heads

Willett et al. (2014) pioneered the use of cross-divide χ contrast to gauge the horizontal motion of drainage divides. According to their method, drainage divides are predicted to move toward the side with a higher χ value to achieve geomorphic equilibrium. However, in a region with spatially variable uplift rates, lithology, or precipitation, χ contrast may fail to reflect the drainage-divide migration (Willett et al., 2014; Whipple et al., 2017; Forte and Whipple, 2018; Wu et al., 2022; Zhou and Tan, 2023). In a tectonically active area, the cross-divide χ contrast can only be used in a small area where rock type, precipitation, and uplift rate are nearly uniform (Willett et al., 2014). Combining the advantages of the χ and Gilbert metrics methods, Zhou et al. (2022a) proposed to use the χ contrast with a high base level to calculate the k_{sn} values at the channel heads on both sides of a drainage divide, and quantified the migration rate of drainage divides at the eastern margin of Tibet.

To reduce the cross-divide difference in uplift rate, precipitation, and rock strength, the Gilbert metrics or χ-comparison method in Zhou et al. (2022a) should compare the parameters of points (slope, relief, elevation, and k_{sn}) on both sides of the divide as closely as possible. As the hillslope area (above the channel head) does not follow Eq. 1 (Stock and Dietrich, 2006; Stark, 2010; Braun et al., 2018; Dahlquist et al., 2018), the channel heads are the closest point to the divide, following Eq. 1. Channel heads, therefore, are suitable for measuring the drainage-divide stability with

476 parameters of the upstream drainage area and channel gradient (Forte and Whipple,

477 2018; Zhou et al., 2022a). However, limited by the resolution of DEM, the location of

478 the channel heads cannot always be accurately identified. The channel head

479 parameters for calculating the migration rates are usually based on empirical values

480 (both sides are the same value) in previous studies (e.g., $A_{cr} = 10^5$ m^2 in Zhou et al.

481 (2022a)), which may induce uncertainties.

482   In this study, we advocate the use of high-resolution DEM to determine a more

483 accurate position and related parameters of the channel head. The use of UAVs to

484 obtain the local DEM has become highly efficient. We advance the theory to calculate

485 the drainage-divide migration rate based on the measured channel-head parameters.

486 With the help of the aerial photography of UAVs and the SfM techniques, it is

487 possible to obtain the high-resolution topography data of drainage divides (Figs. 4A &

488 5A) and get the required parameters (including the exact locations of the channel

489 heads across the drainage divide) through topography analysis. The key parameters

490 includes the exact locations (usually have different A_{cr} across the divides) and the

491 gradients of the channel heads (S_{cr}), which could improve the quantitative research on

492 the drainage-divide migration. Furthermore, the method provides a new avenue to

493 combine with catchment-wide ^{10}Be erosion rate or low-temperature

494 thermochronology data to calculate the migration rate, which has great potential for

495 application in places where some variables are hard to be constrained.

496

4.2 Cross-divide difference in the uplift rate of the channel heads

Although the channel heads across the divide are very close on the spatial scale of an orogenic belt, differential uplift between the channel heads (ΔU_{ch}) could still exist, especially in a tilting horst, such as the Wutai Shan. The cross-divide difference in uplift rate could impact the calculation of the migration rate of drainage divides (Zhou et al., 2022a).

In this study, we quantify the influence of the cross-divide difference in rock uplift rate (ΔU_{ch}) on the calculation of the migration rate of drainage divides at the Wutai Shan, benefiting from the available tectonic and chronological research (Clinkscales et al., 2020) and the newly obtained high-resolution topographic data. In the Wutai Shan horst, ΔU_{ch} across the drainage divide is ~0.008 mm/yr. We estimate the influence of ΔU_{ch} on the drainage-divide migration rate in this case study, which can reduce the error theoretically. If ΔU_{ch} is ignored, the drainage-divide migration rate would decrease by ~4% in the Wutai Shan case. Although ~4% seems to be negligible, such a ratio will increase if the mountain belt is narrower, the tilting uplift is stronger, or the divide is closer to the steady state (i.e., the migration rate is lower) (Whipple et al., 2017; Ye et al., 2022). In other words, the differential uplift may play a significant influence on the measurement of drainage-divide stability in some situations. If we consider an extreme example where the main drainage divide of a tilting mountain range (relatively narrow in width) is at a steady state, the gradient, relief, and elevation of the channel heads (collectively called "Gilbert metrics") (Forte and Whipple, 2018) will show a systematic cross-divide difference in theory. In this

519 case, the drainage divide would be considered unstable if ΔU_{ch} were neglected.

520 Therefore, this study highlights that ΔU_{ch} should be taken into account, either in a

521 qualitative or a quantitative evaluation of the stability of drainage divides using the

522 parameters on the channel heads.

523

524 **4.3 Limitations and uncertainties**

525   This study develops the method to calculate the drainage-divide migration rate

526 based on the measured channel-head parameters. However, uncertainties still exist

527 because of the limitations of this technique. First, we assume the erosion coefficient

528 (K) is the same on both sides of a drainage divide in the derivation of the equations. If

529 there are differences in rock erodibility or precipitation across the divide, uncertainties

530 should exist in the results. Second, the calculation of migration rate is based on the

531 erosion rates at the channel area in this study. However, the occurrence of drainage-

532 divide migration is directly driven by the differential erosion of the hillslope area

533 across the divide, mainly via the processes including landslide, collapse, and diffusion

534 (Stocke and Dietrich, 2006; Stark, 2010; Braun et al., 2018; Dahlquist et al., 2018).

535 Such discontinuous processes in the hillslope area make it challenging to constrain

536 erosion rates over such short timescales. Over a relatively longer period (i.e., spanning

537 multiple seismic and climatic cycles), the erosion rate at the channel head area in this

538 study can be comparable with that at the hillslope area (Hurst et al., 2012; Godard et

539 al., 2020).

540   The accuracy of the data and parameters can also impact the reliability of the

541 results. First, we use the ~~typical~~ uniform values of $n = 1$ and $m/n = 0.45$ in the two

542 natural cases to calculate the migration rate, because it is the best choice to align

543 tributaries with the main stem on the χ-plots in a drainage basin at the northern Wutai

544 Shan (Fig. 6) (Perron and Royden, 2012). If the actual values ~~largely~~ deviate from the

545 assumption, errors would be introduced into the results. For this reason, we have

546 added the cases of $m/n = 0.35$ and 0.55 in Supplementary Materials. Further

547 estimation of these values (Mudd et al., 2018) could improve the accuracy of the

548 results. Second, in the case of the Wutai Shan, we refer to the geological and low-

549 temperature thermochronology studies and assume a 0.50±0.25 mm/yr erosion rate at

550 the northern margin of the Wutai Shan (i.e., the footwall of the North Wutai Shan

551 fault). Combining with the present-day k_{sn}, we calculate the erosion coefficient (K)

552 and derive the migration rates of the drainage divide. If the present-day erosion rate

553 deviates from the assumption, errors would be inevitable in the results. Moreover, the

554 horizontal and vertical errors of the DEM data, as well as the calculation errors in

555 slope, upstream area and channel steepness can also affect the reliability of the results.

556 In the case study of the Yingwang Shan, the lush vegetation may bring errors to the

557 DEM data based on the SfM technology. The application of airborne light detection

558 and ranging (LiDAR) technology may help reduce this error. Future studies should

559 take these challenges into account and overcome them.
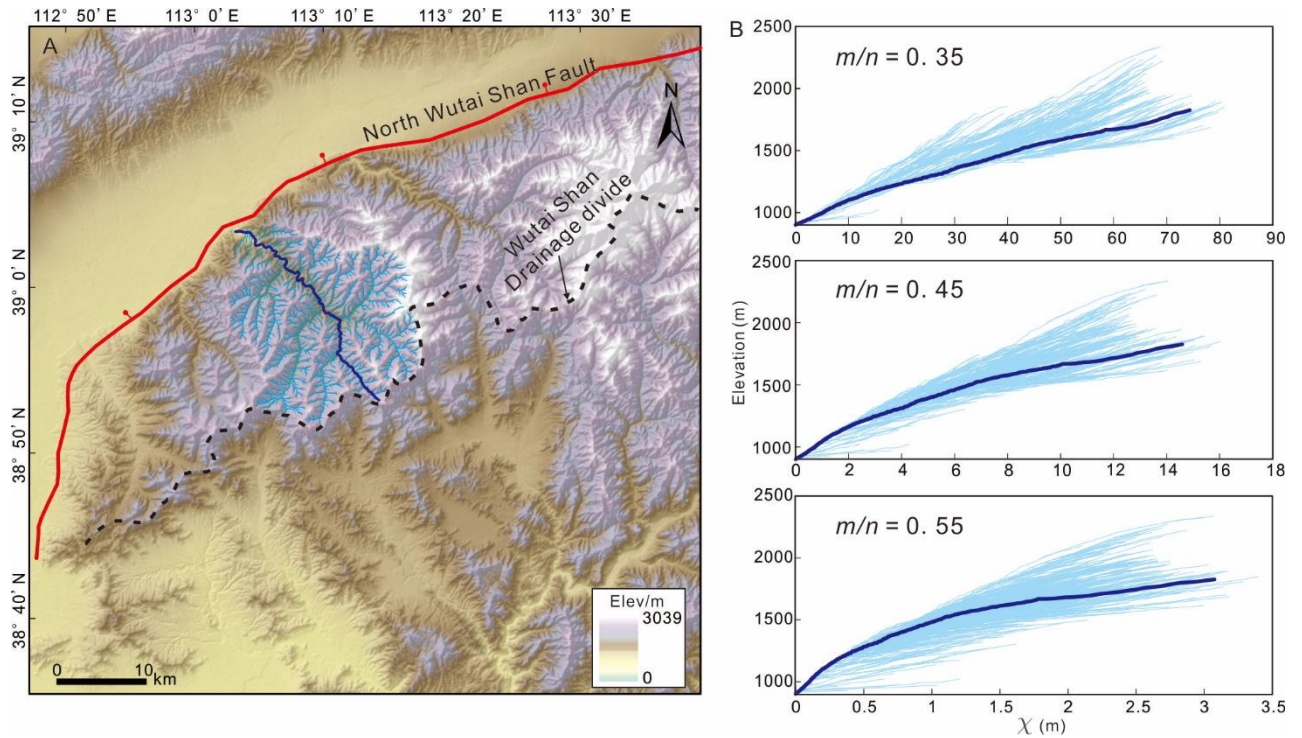
Figure 6. (A) Drainage basin in the northern Wutai Shan. (B) χ-plots of channel profiles in the drainage basin, using $A_0 = 1$ m^2 and $m/n = 0.35$, 0.45, and 0.55. The χ-plots show the best choice of m/n is 0.45, because the tributaries have systematically higher ($m/n = 0.35$) or lower ($m/n = 0.55$) elevations than the main stem for other values of m/n (excluding the channels in the headwaters).

5. Conclusions

We have developed a new method (called the "channel-head-point method") to calculate the migration rate of drainage divides based on channel-head parameters. We have also improved the previously proposed "channel-head-segment method" (Zhou et al., 2022a) to adapt the theory to areas where the parameters of channel-heads can be accurately determined.

573   Using the new methods and high-resolution topographic data, we determined the

574   exact locations of the channel heads on both sides of the drainage divide and

575   quantified the drainage-divide migration rates in two natural cases in North China:

576   Wutai Shan in the Shanxi Rift, and Yingwang Shan in the Loess Plateau. The

577   migration rates of the study sites in the Wutai Shan are 0.21-0.27 mm/yr

578   (northwestward). The rates are close to zero in the Yingwang Shan.

579   Based on the locations of the channel heads and the uplift gradient of the Wutai

580   Shan, we calculated the cross-divide difference in the uplift rate at the channel heads

581   (ΔU_{ch}), which is taken into account in the calculation of the drainage-divide migration

582   rate for the first time. If ΔU_{ch} is overlooked, the drainage-divide migration rate of the

583   study sites in the Wutai Shan will be underestimated by ~4%. Our study highlights

584   that ΔU_{ch} should be considered in the assessment of drainage divide stability based on

585   the cross-divide difference in channel-head parameters.

586

595   greatly improved the paper.

603

604   **References**

605 Authemayou, C., Brocard, G., Delcaillau, B., Molliex, S., Pedoja, K., Husson, L., ~~et~~

606   ~~al.,~~Aribowo, S., and Cahyarini, S. Y.: ~~2018.~~ Unraveling the roles of asymmetric

607   uplift, normal faulting and groundwater flow to drainage rearrangement in an

608   emerging karstic landscape~~.~~, Earth Surface Processes and Landforms, 43(9),

609   1885-1898~~.~~, https://doi.org/10.1002/esp.4363, 2018.

610 Beeson, H. W., McCoy, S. W., and Keen-Zebert, A.~~,~~.: ~~2017.~~ Geometric disequilibrium

611   of river basins produces long-lived transient landscapes~~.~~, Earth Planet Sc. Lett.,

612   475, 34-43~~.~~, https://doi.org/10.1016/j.epsl.2017.07.010, 2017.

613 Bernard, T., Sinclair, H. D., Gailleton, B., and Fox, M.~~,~~.: ~~2021.~~ Formation of

614   Longitudinal River Valleys and the Fixing of Drainage Divides in Response to

615   Exhumation of Crystalline Basement~~.~~, Geophys. Res. Lett., 48~~.~~,

https://doi.org/10.1029/2020gl092210, 2021.

Bian, S., Tan, X., Liu, Y., Fan, S., Gong, J., Zhou, C., Shi, F., and Murphy, M. A.:, 2024. Orographic rainfall drives the Himalaya drainage divide to move north., Geomorphology, 108952., https://doi.org/10.1016/j.geomorph.2023.108952, 2024.

Bonnet, S.,,.:2009. Shrinking and splitting of drainage basins in orogenic landscapes from the migration of the main drainage divide., Nature Geoscience, 2, 766-771., https://doi.org/10.1038/ngeo666, 2009.

Bookhagen, B., and Strecker, M. R.:, 2012. Spatiotemporal trends in erosion rates across a pronounced rainfall gradient: Examples from the southern Central Andes., Earth Planet Sc. Lett., 327-328, 97-110., ttps://doi.org/10.1016/j.epsl.2012.02.005, 2012.

Braun, J.:, 2018. A review of numerical modeling studies of passive margin escarpments leading to a new analytical expression for the rate of escarpment migration velocity., Gondwana Research, 53, 209-224., https://doi.org/10.1016/j.gr.2017.04.012, 2018.

Burbank, D. W., Leland, J., Fielding, E., Anderson, R. S., Brozovic, N., Reid, M. R., and Duncan, C.:, 1996. Bedrock incision, rock uplift and threshold hillslopes in the northwestern Himalayas., Nature, 379, 505–510., https://doi.org/10.1038/379505a0, 1996.

Burbank, D. W., and Anderson, R. S.:, 2001. Tectonic Geomorphology., Blackwell Science, Massachusetts p. 274., 2001.

Carson, M. A., and Kirkby, M. J.: Hillslope form and process, New York, Cambridge

University Press, 475, 1972.

Chen, C.-Y., Willett, S. D., Christl, M., and Shyu, J. B. H.: Drainage basin

dynamics during the transition from early to mature orogeny in Southern

Taiwan, Earth Planet Sc. Lett. 562, https://doi.org/10.1016/j.epsl.2021.116874,

2021.

Clark, M. K., Schoenbohm, L. M., Royden, L. H., Whipple, K. X., Burchfiel, B. C.,

Zhang, X., Tang, W., Wang, E., and Chen, L.: Surface uplift, tectonics,

and erosion of eastern Tibet from large-scale drainage patterns, Tectonics 23, 1-

20, https://doi.org/10.1029/2002tc001402, 2004.

Clift, P. D., and Blusztajn, J.: Reorganization of the western Himalayan river

system after five million years ago, Nature, 438, 1001-1003,

https://doi.org/10.1038/nature04379, 2005.

Clinkscales, C., Kapp, P., and Wang, H.: Exhumation history of the north-

central Shanxi Rift, North China, revealed by low-temperature

thermochronology, Earth Planet Sc Lett 536, 116146,

https://doi.org/10.1016/j.epsl.2020.116146, 2020.

Clubb, F. J., Mudd, S. M., Milodowski, D. T., Hurst, M. D., and Slater, L. J.:

Objective extraction of channel heads from high-resolution topographic data,

Water Resources Research 50, 4283-4304,

https://doi.org/10.1002/2013wr015167, 2014.

Crosby, B. T., and Whipple, K. X.: Knickpoint initiation and distribution within

fluvial networks: 236 waterfalls in the Waipaoa River, North Island, New

Zealand. Geomorphology, 82, 16-38.

https://doi.org/10.1016/j.geomorph.2005.08.023, 2006.

Dahlquist, M. P., West, A. J., and Li, G.: Landslide-driven drainage divide

migration, Geology, 46, 403-406, https://doi.org/10.1130/g39916.1, 2018.

Deng, B., Chew, D., Mark, C., Liu, S., Cogné, N., Jiang, L., O'Sullivan, G., Li, Z.,

and Li, J.: Late Cenozoic drainage reorganization of the paleo-Yangtze

river constrained by multi-proxy provenance analysis of the Paleo-lake Xigeda,

GSA Bulletin, https://doi.org/10.1130/b35579.1, 2020.

DiBiase, R. A., Whipple, K. X., Heimsath, A. M., Ouimet, W. B.: Landscape

form and millennial erosion rates in the San Gabriel Mountains, CA, Earth

Planet Sc. Lett., 289, 134-144, https://doi.org/10.1016/j.epsl.2009.10.036, 2010.

Duvall, A.: Tectonic and lithologic controls on bedrock channel profiles and

processes in coastal California, J. Geophys. Res., 109,

https://doi.org/10.1029/2003jf000086, 2004.

Forte, A. M., and Whipple, K. X.: Criteria and tools for determining drainage

divide stability, Earth Planet Sc. Lett., 493, 102–117,

https://doi.org/10.1016/j.epsl.2018.04.026, 2018.

Forte, A. M., and Whipple, K. X.: Short communication: The Topographic

Analysis Kit (TAK) for TopoToolbox, Earth Surface Dynamics 7, 87–95,

https://doi.org/10.5194/esurf-7-87-2019, 2019.

Forte, A. M., Yanites, B. J., and Whipple, K. X.: Complexities of landscape

evolution during incision through layered stratigraphy with contrasts in rock strength., Earth Surface Processes and Landforms, 41, 1736-1757., https://doi.org/10.1002/esp.3947, 2016.

Fu, B.: 1989. Soil erosion and its control in the loess plateau of China., Soil Use and Management, 5, 76-82., https://doi.org/10.1111/j.1475-2743.1989.tb00765.x, 1989.

Gallen, S. F.: 2018. Lithologic controls on landscape dynamics and aquatic species evolution in post-orogenic mountains., Earth Planet Sc. Lett., 493, 150-160., https://doi.org/10.1016/j.epsl.2018.04.029, 2018.

Godard, V., Dosseto, A., Fleury, J., Bellier, O., and Siame, L.: 2019. Transient landscape dynamics across the Southeastern Australian Escarpment., Earth Planet Sc. Lett., 506, 397-406., https://doi.org/10.1016/j.epsl.2018.11.017, 2019.

Godard, V., Hippolyte, J.-C., Cushing, E., Espurt, N., Fleury, J., Bellier, O., and Ollivier, V.: 2020. Hillslope denudation and morphologic response to a rock uplift gradient., Earth Surface Dynamics, 8, 221-243., https://doi.org/10.5194/esurf-8-221-2020, 2020.

Goren, L., Fox, M., and Willett, S. D.: 2014. Tectonics from fluvial topography using formal linear inversion: Theory and applications to the Inyo Mountains, California., Journal of Geophysical Research: Earth Surface, 119, 1651-1681., https://doi.org/10.1002/2014jf003079, 2014.

Hancock, G. S., and Anderson, R. S.: 2002. Numerical modeling of fluvial strath-terrace formation in response to oscillating climate., GSA Bulletin, 114, 1131-

1142, https://doi.org/10.1130/0016-7606(2002)114<1131:nmofst>2.0.co;2, 2002.

He, C., Yang, C. J., Turowski, J. M., Rao, G., Roda-Boluda, D. C., and Yuan, X. P.: Constraining tectonic uplift and advection from the main drainage divide of a mountain belt, Nat. Commun., 12, 544, https://doi.org/10.1038/s41467-020-20748-2, 2021.

Hilley, G. E., and Arrowsmith, J. R.: Geomorphic response to uplift along the Dragon's Back pressure ridge, Carrizo Plain, California, Geology, 36, https://doi.org/10.1130/g24517a.1, 2008.

Young, H. H., and Hilley, G. E.: Millennial-scale denudation rates of the Santa Lucia Mountains, California: Implications for landscape evolution in steep, high-relief, coastal mountain ranges, GSA Bulletin, 130 (11-12), 1809–1824, https://doi.org/10.1130/B31907.1, 2018.

Hoorn, C., Wesselingh, F. P., Steege, H. T., Bermudez, M. A., and Antonelli, A.: Amazonia Through Time: Andean Uplift, Climate Change, Landscape Evolution, and Biodiversity, Science, 330, 927-931, https://doi.org/10.1126/science.1194585, 2010.

Hoskins, A. M., Attal, M., Mudd, S. M., and Castillo, M.: Topographic Response to Horizontal Advection in Normal Fault-Bound Mountain Ranges, Journal of Geophysical Research: Earth Surface, 128, https://doi.org/10.1029/2023jf007126, 2023.

Howard, A. D., Dietrich, W. E., and Seidl, M. A.: Modeling fluvial erosion on

regional to continental scales, Journal of Geophysical Research: Solid Earth,

99, 13971-13986, https://doi.org/10.1029/94jb00744, 1994.

Howard, A. D., and Kerby, G.: Channel changes in badlands, Geological

Society of America Bulletin, 94, 739, https://doi.org/10.1130/0016-

7606(1983)94<739:CCIB>2.0.CO;2, 1983.

Hu, K., Fang, X., Ferrier, K. L., Granger, D. E., Zhao, Z., and Ruetenik, G. A.:

Covariation of cross-divide differences in denudation rate and χ: Implications for

drainage basin reorganization in the Qilian Shan, northeast Tibet, Earth Planet

Sc. Lett., 562, 116812, https://doi.org/10.1016/j.epsl.2021.116812, 2021.

Hurst, M. D., Mudd, S. M., Walcott, R., Attal, M., and Yoo, K.: Using hilltop

curvature to derive the spatial distribution of erosion rates, Journal of

Geophysical Research: Earth Surface, 117,

https://doi.org/10.1029/2011jf002057, 2012.

Jiao, R., Fox, M., and Yang, R.: Late Cenozoic erosion pattern of the eastern

margin of the Sichuan Basin: Implications for the drainage evolution of the

Yangtze River, Geomorphology, 398, 108025,

https://doi.org/10.1016/j.geomorph.2021.108025, 2022.

Kirby, E., and Whipple, K.: Quantifying differential rock-uplift rates via stream

profile analysis, Geology, 29, 415-418, https://doi.org/10.1130/0091-

7613(2001)029<0415:Qdrurv>2.0.Co;2, 2001.

Kirby, E., Whipple, K., Tang, W., and Chen, Z.: Distribution of active rock

uplift along the eastern margin of the Tibetan Plateau: Inferences from bedrock

channel longitudinal profiles, Journal of Geophysical Research, 108(B4), 2217, https://doi.org/10.1029/2001JB000861, 2003.

Kirby, E., and Whipple, K. X.: Expression of active tectonics in erosional landscapes, J. Struct. Geol., 44, 54-75, https://doi.org/10.1016/j.jsg.2012.07.009, 2012.

Kirkpatrick, H. M., Moon, S., Yin, A., and Harrison, T. M.: Impact of fault damage on eastern Tibet topography, Geology, 48, https://doi.org/10.1130/g48179.1, 2020.

Ma, Z., Zhang, H., Wang, Y., Tao, Y., and Li, X.: Inversion of Dadu River Bedrock Channels for the Late Cenozoic Uplift History of the Eastern Tibetan Plateau, Geophys. Res. Lett., 47, https://doi.org/10.1029/2019gl086882, 2020.

Mandal, S. K., Lupker, M., Burg, J.-P., Valla, P. G., Haghipour, N., and Christl, M.: Spatial variability of 10 Be-derived erosion rates across the southern Peninsular Indian escarpment: A key to landscape evolution across passive margins, Earth Planet Sc. Lett., 425, 154-167, https://doi.org/10.1016/j.epsl.2015.05.050, 2015.

Molnar, P., and England, P.: Late Cenozoic uplift of mountain ranges and global climate change: chicken or egg? Nature, 346, 29-34, https://doi.org/10.1038_346029a0, 1990.

Mudd, S. M., Clubb, F. J., Gailleton, B., and Hurst, M. D.: How concave are river channels? Earth Surface Dynamics, 6, 505-523, https://doi.org/10.5194/esurf-6-505-2018, 2018.

Musher, L. J., Giakoumis, M., Albert, J., Rio, G. D., Rego, M., Thom, G., Aleixo, A.,

Ribas, C. C., Brumfield, R. T., and Smith, B. T.: River network

rearrangements promote speciation in lowland Amazonian birds. Cold Spring

Harbor Laboratory, https://doi.org/10.1126/sciadv.abn1099, 2021.

Perron, J. T., Dietrich, W. E., and Kirchner, J. W.: Controls on the spacing of

first-order valleys. J. Geophys. Res., 113.

https://doi.org/10.1029/2007jf000977, 2008.

Perron, J. T., and Royden, L.: An integral approach to bedrock river profile

analysis. Earth Surface Processes and Landforms, 38, 570-576.

https://doi.org/10.1002/esp.3302, 2012.

Pritchard, D., Roberts, G. G., White, N. J., and Richardson, C. N.: Uplift

histories from river profiles. Geophys. Res. Lett., 36.

https://doi.org/10.1029/2009gl040928, 2009.

Royden, L., Clark, M., and Whipple, K.: Evolution of river elevation profiles

by bedrock incision: Analytical solutions for transient river profiles related to

changing uplift and precipitation rates. Eos Trans. AGU, 81. 2000.

Safran, E. B., Bierman, P. R., Aalto, R., Dunne, T., Whipple, K. X., and Caffee, M.:

2005. Erosion rates driven by channel network incision in the Bolivian Andes.

Earth Surface Processes and Landforms, 30, 1007-1024.

https://doi.org/10.1002/esp.1259, 2005.

Sassolas-Serrayet, T., Cattin, R., Ferry, M., Godard, V., and Simoes, M.: 2019.

Estimating the disequilibrium in denudation rates due to divide migration at the

scale of river basins, Earth Surface Dynamics, 7, 1041-1057,

https://doi.org/10.5194/esurf-7-1041-2019, 2019.

Scheingross, J. S., Limaye, A. B., McCoy, S. W., and Whittaker, A. C.: The

shaping of erosional landscapes by internal dynamics, Nature Reviews Earth &

Environment, 1, 661-676, https://doi.org/10.1038/s43017-020-0096-0, 2020.

Scherler, D., and Schwanghart, W.: Drainage divide networks – Part 2:

Response to perturbations, Earth Surface Dynamics, 8, 261-274,

https://doi.org/10.5194/esurf-8-261-2020, 2020.

Schildgen, T. F., van der Beek, P. A., D'Arcy, M., Roda-Boluda, D., Orr, E. N., and

Wittmann, H.: Quantifying drainage-divide migration from orographic

rainfall over geologic timescales: Sierra de Aconquija, southern Central Andes,

Earth Planet Sc. Lett., 579, 117345, https://doi.org/10.1016/j.epsl.2021.117345,

2022.

Schlunegger, F., Norton, K. P., and Zeilinger, G.: Climatic Forcing on Channel

Profiles in the Eastern Cordillera of the Coroico Region, Bolivia, The Journal of

Geology, 119, 97-107, https://doi.org/10.1086/657407, 2011.

Schwanghart, W., and Scherler, D.: Short Communication: TopoToolbox 2

– MATLAB-based software for topographic analysis and modeling in Earth

surface sciences, Earth Surface Dynamics, 2, 1-7,

https://doi.org/10.5194/esurf-2-1-2014, 2014.

Shelef, E., and Goren, L.: The rate and extent of wind-gap migration regulated

by tributary confluences and avulsions, Earth Surface Dynamics, 9(4), 687-

700, https://doi.org/10.5194/esurf-9-687-2021, 2021.

Shi, F., Tan, X., Zhou, C., and Liu, Y.: Impact of asymmetric uplift on

mountain asymmetry: Analytical solution, numerical modeling, and natural

examples, Geomorphology, 389, 107862,

https://doi.org/10.1016/j.geomorph.2021.107862, 2021.

Shi, W., Dong, S., and Hu, J.: Neotectonics around the Ordos Block, North

China: A review and new insights, Earth-Science Reviews, 200, 102969,

https://doi.org/10.1016/j.earscirev.2019.102969, 2020.

Stark, C. P.: Oscillatory motion of drainage divides, Geophys. Res. Lett., 37,

https://doi.org/10.1029/2009gl040851, 2010.

Stock, J. D., and Dietrich, W. E.: Erosion of steepland valleys by debris flows,

Geological Society of America Bulletin, 118, 1125-1148,

https://doi.org/10.1130/b25902.1, 2006.

Stokes, M. F., Larsen, I. J., Goldberg, S. L., McCoy, S. W., Prince, P. P., and Perron, J.

T.: The Erosional Signature of Drainage Divide Motion Along the Blue

Ridge Escarpment, Journal of Geophysical Research: Earth Surface, 128,

https://doi.org/10.1029/2022jf006757, 2023.

Struth, L., Teixell, A., Owen, L. A., and Babault, J.: Plateau reduction by

drainage divide migration in the Eastern Cordillera of Colombia defined by

morphometry and [10]Be terrestrial cosmogenic nuclides, Earth Surface Processes

and Landforms, 42, 1155-1170, https://doi.org/10.1002/esp.4079, 2017.

Su, P., He, H., Tan, X., Liu, Y., Shi, F., and Kirby, E.: Initiation and Evolution

836   of the Shanxi Rift System in North China: Evidence From Low-Temperature

837   Thermochronology in a Plate Reconstruction Framework, Tectonics, 40,

838   https://doi.org/10.1029/2020tc006298, 2021.

839 Su, Q., Wang, X., Lu, H., and Xie, H.: 2020. Dynamic Divide Migration as a

840   Response to Asymmetric Uplift: An Example from the Zhongtiao Shan, North

841   China, Remote Sensing, 12, https://doi.org/10.3390/rs12244188, 2020.

842 Tucker, G. E., and Bras, R. L.: 1998. Hillslope processes, drainage density, and

843   landscape morphology, Water Resources Research, 34, 2751-2764,

844   https://doi.org/10.1029/98wr01474, 1998.

845 Tucker, G. E., and Slingerland, R.: 1997. Drainage basin responses to climate

846   change, Water Resources Research, 33, 2031-2047,

847   https://doi.org/10.1029/97wr00409, 1997.

848 Vacherat, A., Bonnet, S., and Mouthereau, F.: 2018. Drainage reorganization and

849   divide migration induced by the excavation of the Ebro basin (NE Spain),

850   Earth Surface Dynamics, 6(2), 369-387, https://doi.org/10.5194/esurf-6-369-

851   2018, 2018.

852 Wang, Y., Liu, C., Zheng, D., Zhang, H., Yu, J., Pang, J., Li, C., and Hao, Y.: 2021.

853   Multistage Exhumation in the Catchment of the Anninghe River in the SE

854   Tibetan Plateau: Insights From Both Detrital Thermochronology and

855   Topographic Analysis, Geophys. Res. Lett., 48,

856   https://doi.org/10.1029/2021gl092587, 2021.

857 Waters, J. M., Craw, D., Youngson, J. H., and Wallis, G. P.: 2001. Genes meet

geology: fish phylogeographic pattern reflects ancient, rather than modern,

drainage connections., Evolution, 55, 1844-1851.,

https://doi.org/10.1111/j.0014-3820.2001.tb00833.x, 2001.

Wei, Z., Arrowsmith, J. R., and He, H.:, 2015. Evaluating fluvial terrace riser

degradation using LiDAR-derived topography: An example from the northern

Tian Shan, China., Journal of Asian Earth Sciences, 105, 430-442.,

https://doi.org/10.1016/j.jseaes.2015.02.016, 2015.

Whipple, K. X.: Fluvial landscape response time: how plausible is steady-state

denudation? Am. J. Sci., 301, 313-325, https://doi.org/10.2475/ajs.301.4-5.313,

2001.

Whipple, K. X.:, 2009. The influence of climate on the tectonic evolution of mountain

belts., Nature Geoscience, 2, 97-104., https://doi.org/10.1038/ngeo413, 2009.

Whipple, K. X., Forte, A. M., DiBiase, R. A., Gasparini, N. M., and Ouimet, W. B.:,

2017. Timescales of landscape response to divide migration and drainage

capture: Implications for the role of divide mobility in landscape evolution.,

Journal of Geophysical Research: Earth Surface, 122, 248-273.,

https://doi.org/10.1002/2016JF003973, 2017.

Whipple, K. X., Kirby, E., and Brocklehurst, S. H.:, 1999. Geomorphic limits to

climate-induced increases in topographic relief., Nature, 401, 39-43.,

https://doi.org/10.1038/43375, 1999.

Willett, S. D., McCoy, S. W., Perron, J. T., Goren, L., and Chen, C. Y.:, 2014.

Dynamic reorganization of river basins., Science, 343, 1117.,

https://doi.org/10.1126/science.1248765, 2014.

Willett, S. D., McCoy, S. W., and Beeson, H. W.: Transience of the North American High Plains landscape and its impact on surface water, Nature, 561, 528-532, https://doi.org/10.1038/s41586-018-0532-1, 2018.

Wobus, C., Whipple, K. X., Kirby, E., Snyder, N., Johnson, J., Spyropolou, K., Crosby, B., and Sheehan, D.: Tectonics from topography: Procedures, promise, and pitfalls, Tectonics, Climate, and Landscape Evolution, 55-74, https://doi.org/10.1130/2006.2398(04) , 2006.

Wu, Y., Yang, R., He, C., and He, J.: Caution on determining divide migration from cross-divide contrast in χ, Geological Journal, 57(12), https://doi.org/10.1002/gj.4530, 2022.

Xiong, L.-Y., Tang, G.-A., Li, F.-Y., Yuan, B.-Y., and Lu, Z.-C.: Modeling the evolution of loess-covered landforms in the Loess Plateau of China using a DEM of underground bedrock surface, Geomorphology, 209, 18-26. https://doi.org/10.1016/j.geomorph.2013.12.009, 2014.

Xu, X., Ma, X., and Deng, Q.: Neotectonic activity along the Shanxi rift system, China, Tectonophysics, 219, 305-325, https://doi.org/10.1016/0040-1951(93)90180-R, 1993.

Yan, M.-J., He, Q.-Y., Yamanaka, N., and Du, S.: Location, Geology and Landforms of the Loess Plateau, in: Tsunekawa, A., Liu, G., Yamanaka, N., Du, S. (Eds.), Restoration and development of the degraded Loess Plateau, China, Springer Japan, 3-22, https://doi.org/10.1007/978-4-431-54481-4, 2014.

Yang, R., Suhail, H. A., Gourbet, L., Willett, S. D., Fellin, M. G., Lin, X., Gong, J.,

Wei, X., Maden, C., Jiao, R., and Chen, H.: 2019. Early Pleistocene drainage

pattern changes in Eastern Tibet: Constraints from provenance analysis,

thermochronometry, and numerical modeling., Earth Planet Sc. Lett., 531, 1-

10., https://doi.org/10.1016/j.epsl.2019.115955, 2019.

Ye, Y., Tan, X., and Zhou, C.: 2022. Initial topography matters in drainage divide

migration analysis: Insights from numerical simulations and natural examples.,

Geomorphology, 409, 108266.,

https://doi.org/10.1016/j.geomorph.2022.108266, 2022.

Yin, A.: 2010. Cenozoic tectonic evolution of Asia: A preliminary synthesis.,

Tectonophysics 488, 293-325., https://doi.org/10.1016/j.tecto.2009.06.002,

2010.

Zemlak, T. S., Habit, E. M., Walde, S. J., Battini, M .A., Adams, E. D. M., and

Ruzzante, D. E.: 2008. Across the southern Andes on fin: glacial refugia,

drainage reversals and a secondary contact zone revealed by the

phylogeographical signal of Galaxias platei in Patagonia., Molecular Ecology,

17, 5049-5061., https://doi.org/10.1111/j.1365-294X.2008.03987.x, 2008.

Zeng, X., and Tan, X.: 2023. Drainage divide migration in response to strike-slip

faulting: An example from northern Longmen Shan, eastern Tibet.,

Tectonophysics, 848, 229720., https://doi.org/10.1016/j.tecto.2023.229720,

2023.

Zhao, X., Zhang, H., Hetzel, R., Kirby, E., Duvall, A.R., Whipple, K. X., Xiong, J.,

Li, Y., Pang, J., Wang, Y., Wang, P., Liu, K., Ma, P., Zhang, B., Li, X., Zhang, J., and Zhang, P.: Existence of a continental-scale river system in eastern Tibet during the late Cretaceous-early Palaeogene, Nat. Commun., 12, 7231, https://doi.org/10.1038/s41467-021-27587-9, 2021.

Zhou, C., Tan, X., Liu, Y., Lu, R., Murphy, M. A., He, H., Han, Z., and Xu, X.: Ongoing westward migration of drainage divides in eastern Tibet, quantified from topographic analysis, Geomorphology, 402, 108123, https://doi.org/10.1016/j.geomorph.2022.108123, 2022a.

Zhou, C., Tan, X., Liu, Y., and Shi, F.: A cross-divide contrast index (C) for assessing controls on the main drainage divide stability of a mountain belt, Geomorphology, 398, 108071, https://doi.org/10.1016/j.geomorph.2021.108071, 2022b.

Zhou, C., and Tan, X.: Quantifying the influence of asymmetric uplift, base level elevation, and erodibility on cross-divide χ difference, Geomorphology, 427, 108634, https://doi.org/10.1016/j.geomorph.2023.108634, 2023.

Zondervan, J. R., Stokes, M., Boulton, S. J., Telfer, M. W., and Mather, A. E.: Rock strength and structural controls on fluvial erodibility: Implications for drainage divide mobility in a collisional mountain belt, Earth Planet Sc. Lett., 538, https://doi.org/10.1016/j.epsl.2020.116221, 2020.